Millimetre Wave Power Measurement

A thesis

submitted in partial fulfilment

of the requirements for the Degree

of

Masters of Engineering

at the

University of Waikato

by

Mark H. Jones

KO TE TANGATA

THE UNIVERSITY OF
WAIKATO
Te Whare Wānanga o Waikato

University of Waikato

2010

Abstract

There is currently no traceable power sensor for millimetre wave frequencies above 110 GHz. This thesis investigates a novel approach to remove this limitation by combining the placement of a uniquely designed microchip directly in waveguide. The design of the chip is novel in that it does not rely on a supporting structure or an external antenna when placed in the waveguide. The performance of the design was primarily analysed by computer simulation and verified with the measurement of a scale model. The results show that it is feasible to measure high frequency power by placing a chip directly in waveguide. It is predicted that the chip is able to absorb approximately 60% of incident power. Any further efficiency would require modification of the chip substrate. However, this proposed design should allow the standards institutes a reference that will enable the calibration of equipment to beyond 110 GHz.

Acknowledgements

Firstly, I wish to thank my supervisor, Professor Jonathan Scott, who encouraged me to take this step of academia. I have done many things during the course of this project that my confidence would otherwise have prevented me from doing, achieved simply because he believed I could.

Secondly, thank you Eric Brekenridge of Agilent Technologies from Scotland. The feedback and support delivered amidst tough environmental and economic times was extremely valuable.

Thank you Agilent Technologies Inc. for the University Research Grant, the precursor to this research.

I would also like to thank Dylan Williams and Kate Remley of NIST (Boulder, CO.) for the tour of the NIST facility and showing me your amazing home. Thank you Tom Crowley, also from NIST, for showing me your workshop and national standards calibration.

Thank you Kent and Marion Larson for accepting me into your home, feeding me and showing me the surrounding Santa Rosa countryside while I visited NIST and attended a conference.

Thank you to my mother, Gina McFarlane, for proof-reading this work.

And last but not least, Sarah van der Veer, my partner, for dealing with my lack of focus on things other than microchips, millimetre waves and waveguides over the past year.

Statement of Originality

The design of the microchip and its features are that of my supervisor's, Professor Jonathan Scott.
The description of S-parameters has largely been taken from K. R. Demarest, 1998 [6].
The alternative concept featured in the appendix was a separate investigation done as part of my masters degree. It has been included as it has some relevance to the project.
The design of the two port clamshell model is original.
The design of the bulkhead is original.
The use of loss factor to interpret the performance of the sensor is original, although the derivation of the term itself is not [3].

Contents

List of Figures

Chapter 1

Introduction

The lack of a traceable power sensor above 110 GHz, part of the millimetre wave range of frequencies (30–300 GHz), presents a design challenge to anyone requiring such a sensor. There is growing interest in the millimetre wave band from communications, security, military and automotive industries.[13, 9, 8, 19]

The aim of this study is to investigate a design of thermocouple power sensor, based in the design of W. Jackson, for use in waveguide. The design will comprise of a microchip on which thermal dissipation and sensing mechanisms will be deposited. This chip will then be housed directly in a waveguide section contained within a bulkhead that will also provide connection to an external meter unit. The meter unit will apply any necessary corrections to the data as well as display results to the user.

Although, the idea of a finline thermocouple power sensor has been patented [18], placing all of the components including the antenna on a chip packaged directly in waveguide without a supporting structure is new.

Research has also been done on the packaging of a chip directly in waveguide [11] but has not been applied to thermal power sensors. The work presented an idea of offsetting the chip in order to increase its broadband match, which was tried in this investigation.

A potential problem with the design of a finline thermal power sensor is its ability to absorb a sufficient amount of power from the waveguide. Having such limited space for a receiving element (antenna) on the chip could mean that the sensor cannot capture enough energy to make measurements. The ideal shape of a chip for this purpose would be long, giving ample room for an adequate antenna. Unfortunately, the longer a chip becomes the higher the probability it has of breaking; a chip approximately twice as long as it is high is the conventional limit. Minimising chip area while maximising its electromagnetic performance is necessary as wafer space is expensive.

Samples of the chip, designed for this sensor, are held by my supervisor, Professor Scott. These chips, which we have termed Fin-cat, were manufactured to utilise spare wafer space with the intention that they may one day be used for making such a sensor. However, the design has not been tested as this would be an involved process requiring equipment that is unavailable at present and a very carefully crafted bulkhead.

In order to determine how well the design of chip will work it will be simulated in a section of waveguide. Verification of the simulated data will be done by measuring a scale model of the setup. This data should give an indication of how well the sensor will work and therefore determine whether or not it is a feasible approach to the problem of power measurement over 110 GHz. This study also identifies the limiting factors in the design of the chips we hold and suggests area for future research.

Chapter 2

History and Review

2.1 Power Sensors

The three most popular types of power sensor on the market today are the thermistor, diode and thermocouple sensors. Their typical measurement characteristics are summarised in table 2.1

	Thermistor	Diode	Thermocouple
Sensitivity	-30 dBm (1μW)	-70dBm (100pW)	-30 dBm (1μW)
Ease of calibration	Easy	Difficult	Slightly involved
Accuracy	$\approx$ 1%	Input Dependent	less than 1%

Table 2.1: Brief comparison of sensor technologies

During the 1950s and 60s thermistor type sensors were the main choice for microwave and radio frequency power measurement. However, in more recent years diode and thermocouple sensors have captured the bulk of this market.[20] Thermistor type sensors are used by standards institutes as they are much easier to calibrate than the alternatives.

Diode type sensors are more sensitive than both thermocouple or thermistor sensors, but their accuracy is usually lower. Diode sensors are unable to guarantee true root mean square (RMS) output as they suffer from nonlinearities when the power level exceeds its square law range. This means that diode sensors only work well when the signal being measured has small variations of amplitude. Thermocouple and thermistor type sensors are generally more accurate than diode sensors as they can be calibrated to a higher precision. They also give true RMS measurements as they are based on thermal dissipation.

2.1.1 The thermocouple power sensor

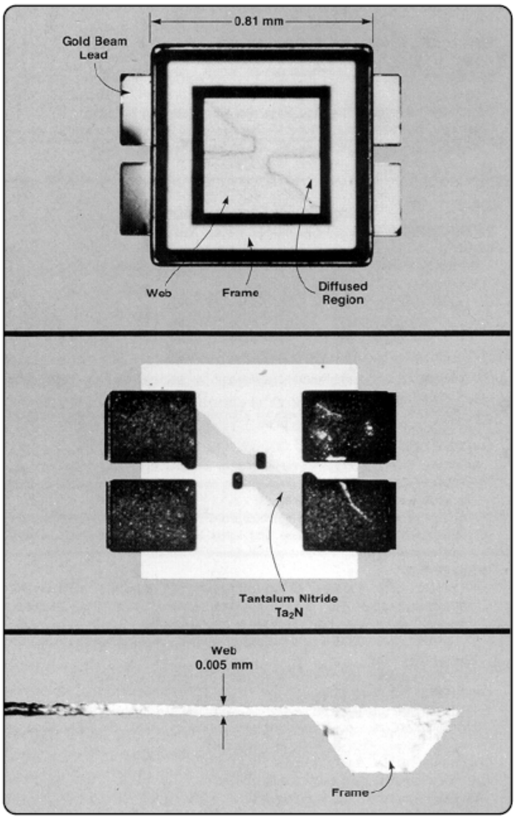

Figure 2.1: Photo-micrograph of the structure of Jackson's thermocouple chip on a thin silicon web[20]

In 1974, Weldon Jackson of Hewlett Packard published a paper detailing a revolutionary design of a thermocouple power sensor [10]. This design used thermocouples that were deposited directly onto a microchip, utilising the semiconductor substrate as part of the thermocouple. These thermocouples provided excellent sensitivity because of a high Seebeck coefficient obtained from their metal-semiconductor junctions. This integrated thermocouple technology was eventually adopted by all major manufacturers of thermal power sensors [5, 18, 12]. Jackson's design also managed to increase sensitivity by removing substrate from the underside of the chip. This created a thin web-like layer upon which hot thermocouple junctions lay.

The chip contains two thermocouples, each connected to two connection pads (see figure 2.1). These thermocouples are also the resistance through which incident power is dissipated. This dissipation heats the centre of the chip, where the resistance is the greatest due to narrowing of the thermocouple tracks. As the centre of the chip is made from a very thin layer, a much faster temperature response and higher sensitivity is achieved. The outside of the chip has not had its substrate etched away and therefore remains much cooler; this area is used to keep the cold thermocouple junctions cool, maximising temperature difference between junctions.

2.2 Additional Technology

This section is intended to give a brief overview of existing technologies and measurement parameters. It has been included to provide the necessary background for further discussion.

2.2.1 Waveguide

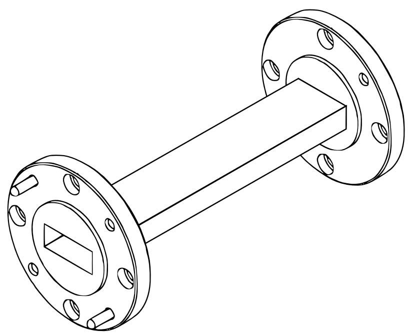

Figure 2.2: Diagram of a rectangular waveguide section showing standard flanges.

Over 110 GHz coaxial cable is extremely lossy, placing a heavy toll on its use. Waveguide is an alternative to coaxial cable that is better suited for transmission of extremely high frequency electromagnetic waves. A waveguide is a dielectric or conductive pipe through which waves of energy are guided rather than conducted. The physical dimensions of a waveguide are inversely proportional to the frequency of its operation. This means that a waveguide designed for low frequencies will, by necessity, be large. For example, a waveguide for use at 1 MHz would need to be 150m wide and 75m high. This makes it generally unsuitable for low frequency applications below 1 GHz.[15] This application of waveguide technology in the design of a thermal power sensor will utilise rectangular waveguide, an example of which is shown in figure 2.2.

2.2.1.1 Modes of propagation

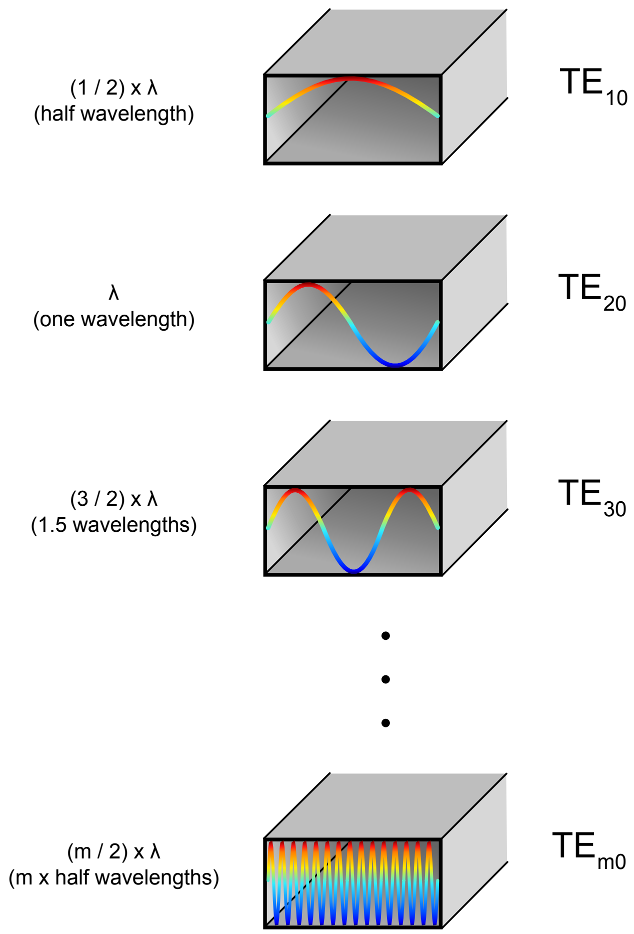

Figure 2.3: Diagram showing the geometry of various modes of propagation in rectangular waveguide.

The width of a waveguide determines the largest wavelength, and therefore the lowest frequency, it will propagate. This frequency is called the fundamental mode cutoff frequency, f_c. Above a certain thresholds, determined by the waveguide geometry, energy becomes free to propagate in different modes. In order to understand how modes arise it helps to see how electromagnetic waves occupy the space within a waveguide. Figure 2.3 shows how the first few modes fill the guide; the coloured line represents the electric field of an electromagnetic wave. These modes are denoted TE_{mn} where m and n represent the number of half wavelengths that fit either horizontally (m) or vertically (n) in the guide. Once the frequency of energy in the guide exceeds a higher order mode cutoff frequency then the energy will propagate in that higher order mode. The waveguide is still free to propagate lower order modes simultaneously. The electric fields can therefore become very messy if frequencies are not managed properly.

When frequencies increase but no mode change occurs, wavelengths become smaller in the direction of propagation, as would be seen by looking into the side of the guide. Figure 2.4 and 2.5 show the electric fields of TE_{10} and TE_{01} waves as they propagate down a section of waveguide.

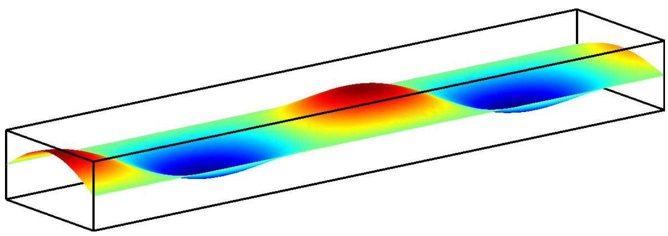

Figure 2.4: Simulation showing a TE_{10} waveform inside a waveguide section.

Different modes propagate at different velocities; therefore permitting more than one mode would cause signals to disperse. To avoid this, a waveguide should be operated exclusively in its TE_{10} mode. This means that the transmission of energy should not reach the cutoff frequencies of either TE_{20} ($f_{c(TE_{20})}$) or TE_{01} ($f_{c(TE_{01})}$), which are the cutoff frequencies of the first higher

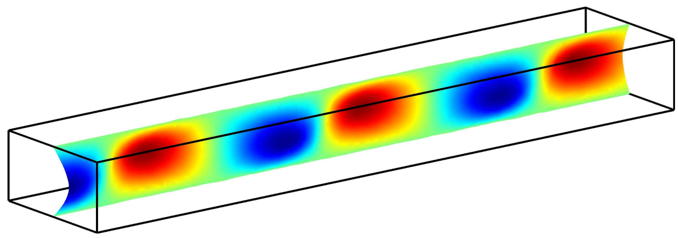

Figure 2.5: Simulation showing a TE_{01} waveform inside a waveguide section.

order modes above TE_{10}.

2.2.1.2 Cutoff frequencies

The cutoff frequency of each mode is calculated from the dimensions of the cross-section of a waveguide as follows:

$$f_c = c\sqrt{\left(\frac{m\pi}{a}\right)^2 + \left(\frac{n\pi}{b}\right)^2} \tag{2.1}$$

Where a and b are the width and height of a waveguide cavity, respectively, and c is the speed of light in a vacuum. Figure 2.6 shows the first six modes for the WR-6 waveguide standard (110–170 GHz), its dimensions are 1.651mm (a) by 0.8255 (b).

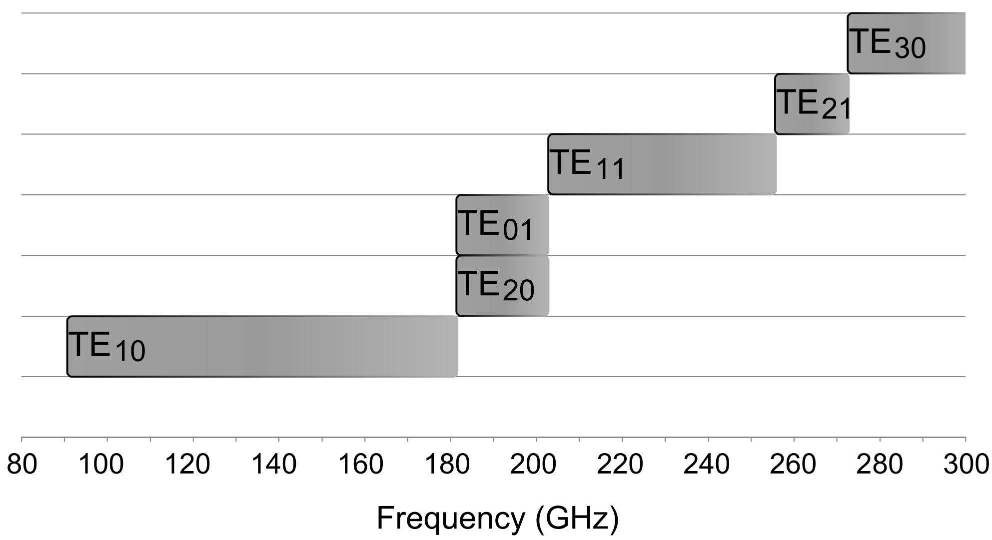

Figure 2.6: Diagram showing the range of frequencies covered by the first six modes of propagation in WR-6 waveguide.

Using equation 2.1, the cutoff frequencies for the three relevant modes of operation can be calculated. These higher modes (TE_{20} and TE_{01}) mark the top end of the waveguides useful frequency range. The following calculations are for a waveguide having a 2: 1 width to height ratio, common for rectangular waveguides.

$$\begin{aligned} f_{c(TE_{10})} &= c\sqrt{\left(\frac{\pi}{a}\right)^2} \\ &= \frac{\pi c}{a} \end{aligned} \tag{2.2}$$

$$\begin{aligned} f_{c(TE_{20})} &= c\sqrt{\left(\frac{2\pi}{a}\right)^2} \\ &= \frac{2\pi c}{a} \end{aligned} \tag{2.3}$$

$$\begin{aligned} f_{c(TE_{01})} &= c\sqrt{\left(\frac{\pi}{b}\right)^2} \\ &= \frac{\pi c}{b} \qquad \text{(b = 0.5a)} \\ &= \frac{2\pi c}{a} \end{aligned} \tag{2.4}$$

The preceding equations show that using a 2: 1 height to width ratio gives the largest possible single mode bandwidth. For instance, if the waveguide was taller; $f_{c(TE_{01})}$ would drop in frequency, alternatively if the waveguide was wider; $f_{c(TE_{20})}$ would drop in frequency. These equations also show that the frequency at which the waveguide first begins to multimode is exactly twice that of the fundamental mode cutoff frequency ($f_{c(TE_{10})}$).

Generally, the operational frequency range of a waveguide does not extend to its cutoff frequencies. The TE_{10} and TE_{20} cutoff frequencies for WR-6 waveguide are 90.79 GHz and 181.6 GHz respectively, however the waveguide is only operated between 110–170 GHz.

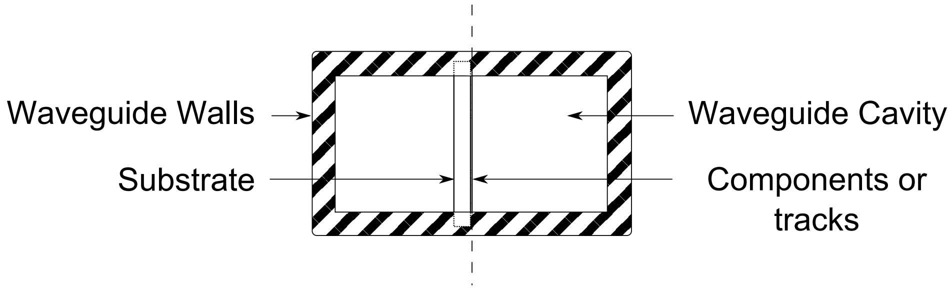

Figure 2.7: Cross-section of waveguide showing a finline structure.

2.2.2 Finline

Finline is the name given to a method of placing components inside a waveguide, usually on a dielectric support. The geometry of finline is shown in figure 2.7. Finline can be used to add components such as filters, antennas and diodes directly into a waveguide cavity. It provides a convenient way of placing such components in circuit without the need to resort to coaxial cable or other more common transmission mediums. The use of finline in waveguides have been studied [14, 17, 4, 1, 2].

2.3 Scattering parameters

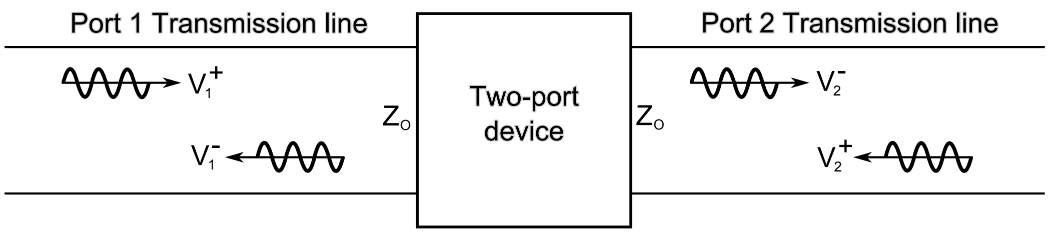

Figure 2.8: Ingoing and outgoing voltage waves at the ports of a two-port device.

This section is intended to provide a brief description of scattering parameters, which are the underlying measurements for loss factor calculations. Scattering parameters, or S-parameters, are a good way of representing the characteristics of RF circuits. They are introduced by figure 2.8 which represents an arbitrary two-port device. Here, both ports are transmission lines with characteristic impedances of Z_0. As is always the case on transmission lines, voltage waves can propagate in either direction. The incoming and outgoing voltage phasors at port 1 are denoted using V_1^+ and V_1^- respectively. Similarly, V_2^+ and V_2^- are the phasors of the incoming and outgoing voltage waves at port 2. The S-parameters relate the waves according to the following equations:

$$V_1^- = S_{11}V_1^+ + S_{12}V_2^+ \tag{2.5}$$

$$V_2^- = S_{21}V_1^+ + S_{22}V_2^+ \tag{2.6}$$

From the preceding equations each S-parameter is expressed in terms of the ratio of an outgoing and incoming voltage phasors:

$$S_{11} = \frac{V_1^-}{V_1^+} \qquad \text{when } V_2^+ = 0 \text{ (Port 2 matched)} \tag{2.7}$$

$$S_{12} = \frac{V_1^-}{V_2^+} \qquad \text{when } V_1^+ = 0 \text{ (Port 1 matched)} \tag{2.8}$$

$$S_{21} = \frac{V_2^-}{V_1^+} \qquad \text{when } V_2^+ = 0 \text{ (Port 2 matched)} \tag{2.9}$$

$$S_{22} = \frac{V_2^-}{V_2^+} \qquad \text{when } V_1^+ = 0 \text{ (Port 1 matched)} \tag{2.10}$$

From the preceding equations it can be seen that each S-parameter is the ratio of an outgoing wave to an incoming wave, under the restriction that one of the ports is terminated with a non-reflecting (i.e., matched) load. S-parameters are denoted S_{ij}, with the i and the j representing the observed port and active port numbers respectively. For example, S_{11} represents the ratio of energy reflected from port one to energy incident on port one, called the input reflection coefficient. S_{21} is the ratio of energy transmitted to port two when port one is active, called the forward transmission coefficient.

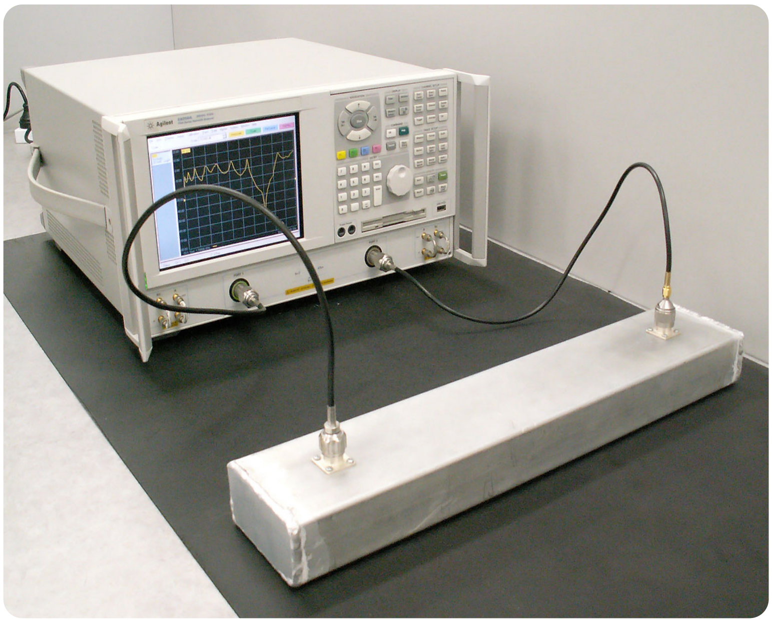

Figure 2.9: Agilent E8358A VNA measuring S-parameters of an empty waveguide cavity.

S-parameters are frequency dependant, meaning that they change depending on the frequency of waves used to take the measurement. Therefore, it is necessary to make measurements over a range of frequencies to better characterise the device under test. A Vector Network Analyser (VNA) is such an instrument able to measure S-parameters across a wide range of frequencies. The University of Waikato possesses an Agilent E8358A vector network analyser that can measure S-parameters up to a frequency of 9 GHz. A photo of this unit can be seen in figure 2.9.

2.3.1 Loss Factor

By applying a calculation to the measured S-parameters a quantity that is termed loss factor results. This quantity represents the amount of energy lost to the device in question, which in this instance is the sensor. It is simply the difference between input power and power that is both reflected and transmitted at the input and output ports correspondingly [3]. Loss factor is used for devices that have two or more ports, which the sensor wont. However, analysis of the sensor was done using two-port models and simulations to get an idea of how much energy escapes behind the chip, something that a one port model or simulation would not be able to show. Loss factor gives the convenience of interoperating data as if it were a one-port device.

2.3.1.1 Derivation

Derivation of the loss factor is begun by converting each S-parameter, which represent a ratio of voltages, into a ratio of powers. These are denoted as $S_{ij_{POWER}}$.

Converting these voltages into powers via Ohms law and the power equation ($P = VI$) results in:

$$\begin{aligned} S_{11_{POWER}} &= \frac{(V_1^-)^2}{Z} \frac{Z}{(V_1^+)^2} \\ &= \frac{(V_1^-)^2}{(V_1^+)^2} \\ &= \left| \frac{V_1^-}{V_2^+} \right|^2 \\ &= |S_{11}|^2 \end{aligned} \tag{2.11}$$

Therefore, squaring an S-parameter turns it from a ratio of voltages into a ratio of powers, applicable to each S-parameter. The next step is to determine the amount of power that was not reflected nor transmitted. As S-parameters are normalised reflection and transmission coefficients, this is a straightforward sum of inputs and outputs:

$$LossFactor = 1 - |S_{11}|^2 - |S_{21}|^2 \tag{2.12}$$

Maximising the loss factor across the 110–170 GHz band should improve sensor performance if this loss is the result of thermal dissipation, which it is assumed to be.

Chapter 3

Design

In this chapter the design of both the bulkhead and the chip are introduced. Once an indication of the designs performance was ascertained, other chip designs were tried that are shown at the end of this chapter.

3.1 Bulkhead

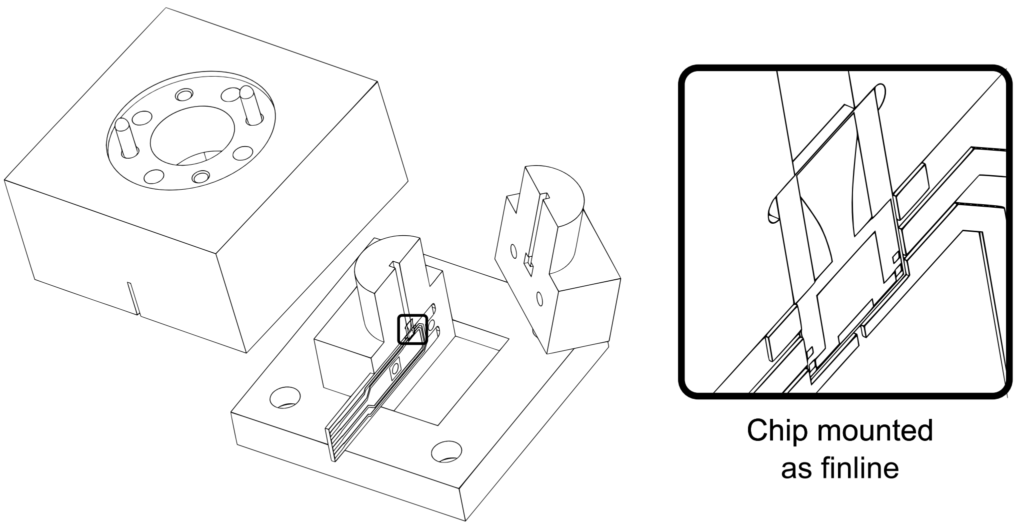

Figure 3.1: Diagram of the proposed clamshell bulkhead design, showing the chip mounted as a finline component.

The bulkhead will house the chip and provide the waveguide cavity. As the chip is to be packaged directly in the waveguide, as opposed to being mounted on a finline support, the design of the bulkhead becomes an increasingly important part of the sensor. As the dimensions of the chip are small, approximately 1.5mm x 3mm, the bulkhead would have to be made extremely precisely in order to minimise unwanted interference as well as ensuring correct placement of the chip.

3.1.1 Materials

To prevent excessive power loss and reduce manufacturing costs the bulkhead could be made primarily from copper with a small amount of silver and gold. Copper is used as it is relatively cheap and offers good thermal and electrical conductivity. The copper would then be laminated with silver [21]. The silver layer would be approximately 0.8μm thick, approximately five skin depths thick at 170 GHz. This would therefore account for almost all electrical conduction in the waveguide walls. Silver is used as it has the highest electrical conductivity of any known metal. The final layer, gold, would then be flashed as thinly as possible over the silver to prevent it from oxidising.

3.1.2 Design

Professor Scott envisioned that the bulkhead would be a clamshell design, allowing an easy way to manufacture the cavity and insert the chip. A concept of this bulkhead is depicted in figure 3.1. The design features a standard WR-6 waveguide flange, used to attach the sensor to other WR-6 waveguide devices. The bulkhead will be a one-port device, terminated by the chip followed by a reflective wall. If the distance between the back wall and the chip is set correctly performance of the sensor will be increased, as the chip will reclaim a portion of energy that was lost. An approximate calculation puts this distance at about 0.85mm.

3.1.3 Assembly

Figure 3.2 depicts the bulkhead assembly process.

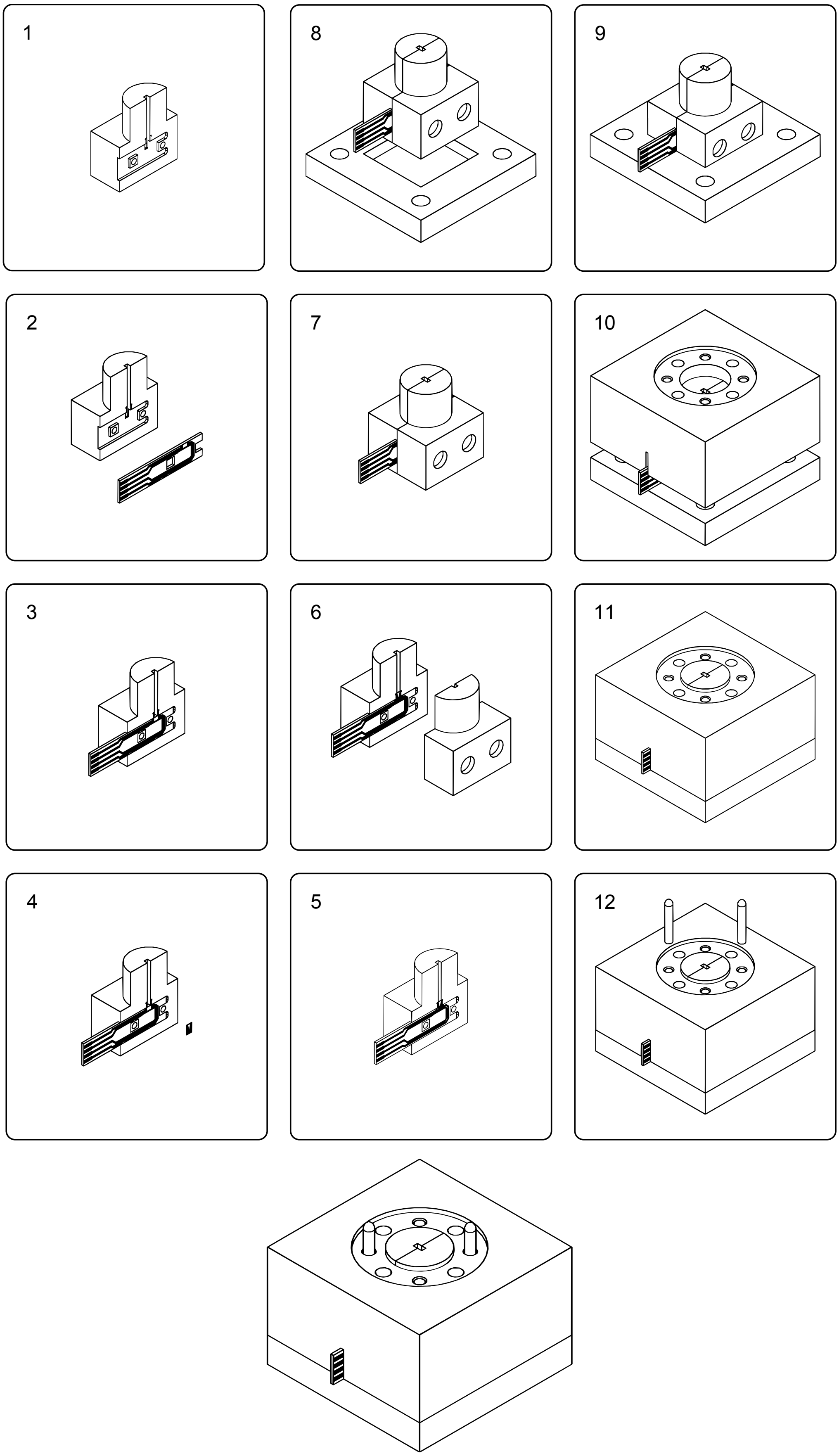

Figure 3.2: Diagram showing assembly of bulkhead.

3.2 Chips

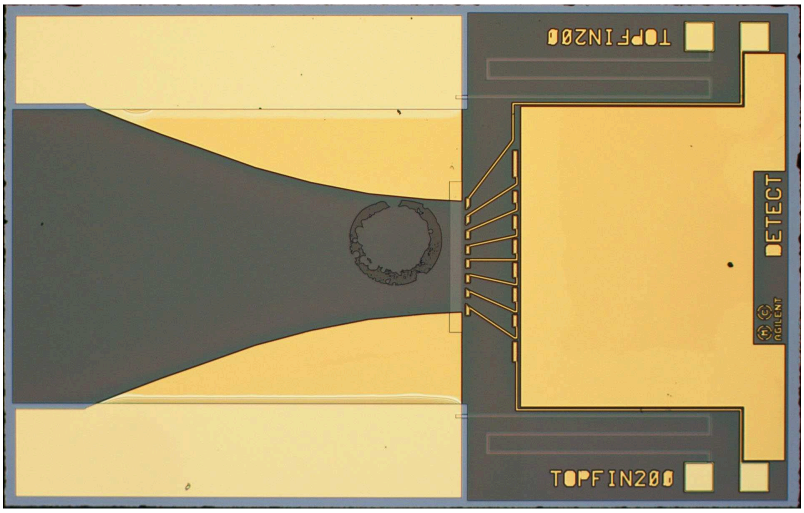

Figure 3.3: Micrograph of a Fin-cat chip.

The Fin-cat chips, which Professor Scott designed for this sensor, represent a good starting point for the design of the ideal chip, one of these is shown in figure 3.3. The dimensions of the chips are 2.14mm x 1.35mm x 0.1mm, which is taller than the height of the waveguide (0.8255mm) to allow it to be supported by grooves in the waveguide cavity. The mating of the chip to these grooves will also provide a thermal escape route for heat build-up on the chip.

3.2.1 Components

The chips consist of an antenna, thin-film resistor, thermocouples, heat sink and pads with connecting tracks, as shown in figure 3.4. The heat sink, antenna, connection pads and tracks are all made from a thin layer of gold deposited on the surface of the chip, 2μm thick.

3.2.1.1 Antenna

The antenna is simply the two fins that protrude inwards linked by a thin-film resistor. The wide rectangles on the outside of the fins provide a point of contact between the fins and the inside of the grooves in the waveguide walls.

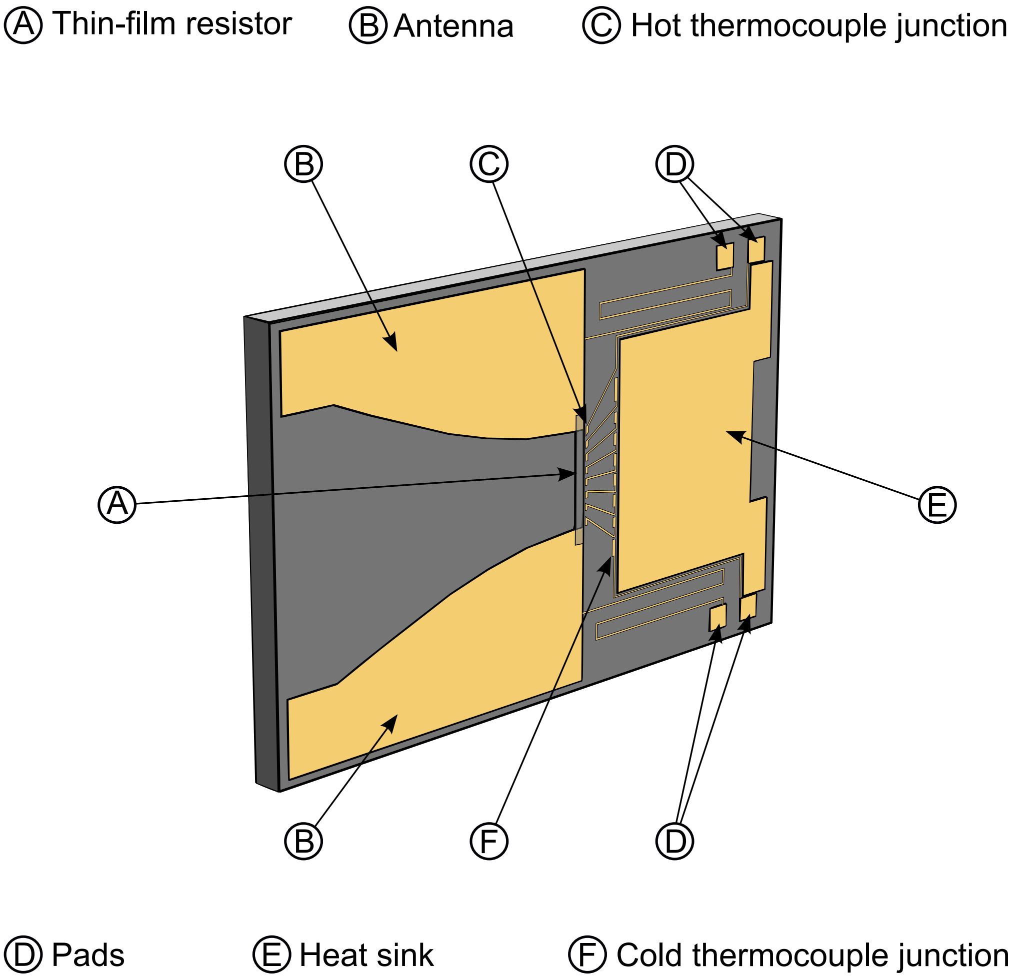

Figure 3.4: Block diagram of the Fin-cat chip.

As the fins are so thin, and frequencies so high, they will have a considerable resistance. This resistance will increase the amount of loss that occurs, but in a way that will detract from the performance of the sensor. This is because the resistance will occur before energy reaches the resistor.

3.2.1.2 Thermocouples

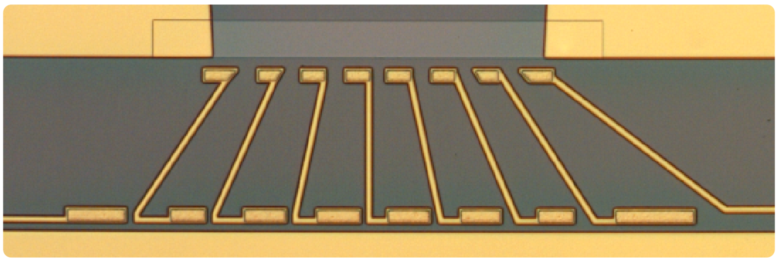

Figure 3.5: Micrograph of the eight thermocouples, in series, on the Fin-cat chip. The thin-film resistor (top) and heat sink (bottom) can also be seen.

The thermocouples described by Jackson used a diffused silicon substrate region together with a layer of tantalum nitride. The thermocouples used on the Fin-cat chips are deposited on a gallium arsenide substrate and do not double as the resistance through which energy is dissipated. Separating the resistive element from the thermocouples gives greater flexibility in the design of both the resistance and the thermocouples. The chip samples have eight thermocouples in series with one another in order to increase sensitivity.

3.2.1.3 Resistor

A focus of this study is to determine the optimum value of resistance between the antenna fins. Selecting the correct value of resistance between the fins will increase the match between the chip and the waveguide. A better match allows more power to be dissipated through the resistor increasing the amount of heat produced per unit of power available to the chip. The match is determined by the difference of impedance between the antenna and the waveguide; the lower the difference the better the match.

The impedance of the waveguide (η_1) is given by:

$$\eta_1 = \frac{Z_0}{\sqrt{1 - \left(\frac{f_c}{f}\right)^2}} \tag{3.1}$$

Where Z_0 is the impedance of free space, f is frequency and f_c in this case will be the TE_{10} mode cutoff frequency, as given by equation 2.2.

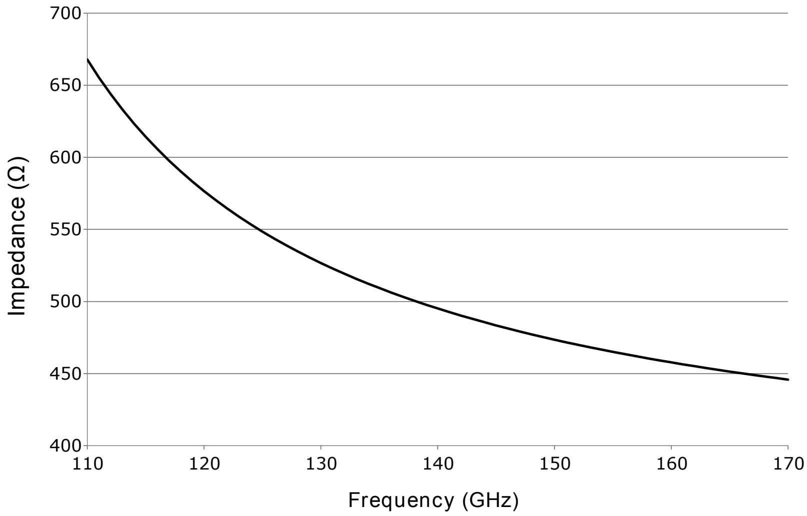

Figure 3.6: Graph of impedance vs. frequency of an air-filled waveguide section.

Figure 3.6 shows the impedance of a WR-6 waveguide as a function of frequency. It shows that there is a large variation in impedance across the waveguides operational frequency range. This makes the selection of an ideal resistor more complicated as no one value would give a good match at all points. On top of this resistance, the characteristic impedance of the fin-antennas plus any resistance arising from the finite conductivities gold used to make the fins must also be taken into account.

3.2.1.4 Back-etching

The Fin-cat chips have not had substrate etched away to create the thin web-like layer like in Jackson's design. However, this methodology of substrate removal is directly applicable to this design bringing with it increased sensitivity and reduced response time. Jackson's chip used silicon where we are using gallium arsenide (GaAs). As a result, there may need to be some alterations made to the design or fabrication equipment in order to accommodate the change of substrate material.

Chapter 4

Computer Simulation

Simulations were used to see how well a sensor having ideal properties, such as perfect conductivities and geometries, would perform. If the simulator predicted that there was no way that power would make it into the resistor, because of the shape or size of the antenna, the design could be destined to fail. Fortunately, the simulators showed that the design should not only work but perform well. The results of all simulations are shown in chapter 6.

4.1 Limitations

Electromagnetic simulators work by taking a model of the problem and breaking it up into smaller elements. This is called 'meshing' and results in a three dimensional structure built entirely from tetrahedrons, or similar volumetric shapes. This meshing becomes an issue for very thin features in a model where the ratio of dimensions is large. As a feature in the model becomes thinner, the number of mesh elements required to represent that feature increases exponentially. This is a serious problem when modelling the fins of the chip as they are 826 000 times thinner than the width of the waveguide cavity and 500 times longer than their thickness. As a result, simulations had to be done with a fin thickness of 10μm, instead of the actual thickness of 2μm, and perfectly conducting boundaries for both the fins and waveguide walls. This will change the answer due to the fins being thicker than they really are, but was

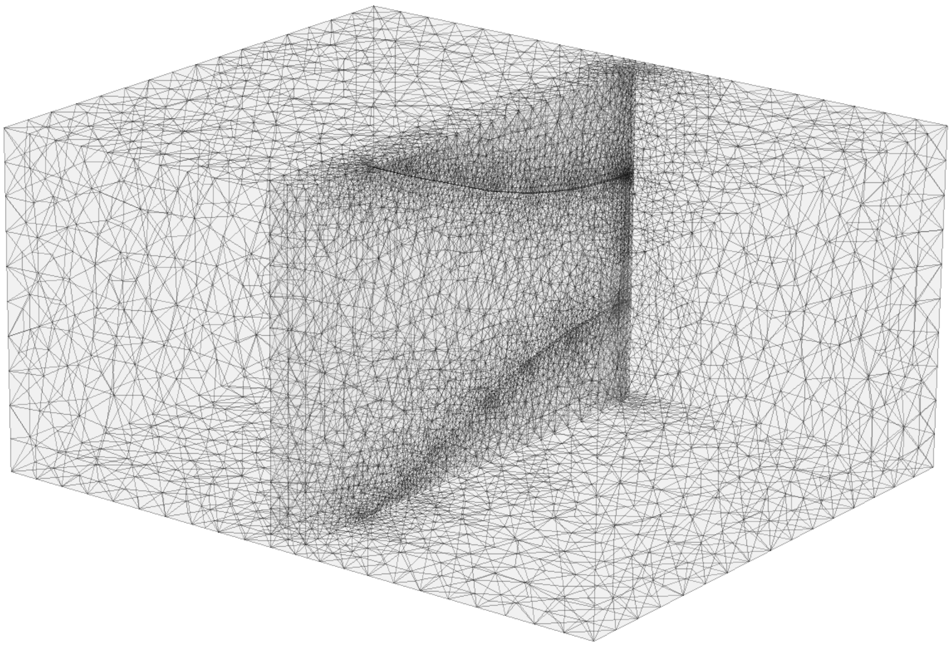

Figure 4.1: Screenshot of the meshed model showing the density of mesh elements.

a necessary step if simulations were to be conducted at all. By making the walls and fins perfectly conducting, the area outside the walls and inside the fins can be completely removed from the model as they will have no effect on the answer, making the model much leaner.

4.2 The Simulations

The base simulation setup is shown in figure 4.2. This was the basis for many of the simulations as most only differed by resistance values or chip placement and no new geometry. The centring of the chip actually describes the position of the fins relative to the waveguide, while the substrate is slightly to one side. Any offset is in the direction that moves the substrate closer to the waveguide wall. Simulations were first done in order to characterise the Fin-cat chips. This used a resistance of 200Ω and no offset. Once this was completed and compared to measured data, simulations were conducted with the chip placed at various offsets, much as described by [11]. The best offset was determined by the simulator to be 180μm, which had the highest average loss and smoothest

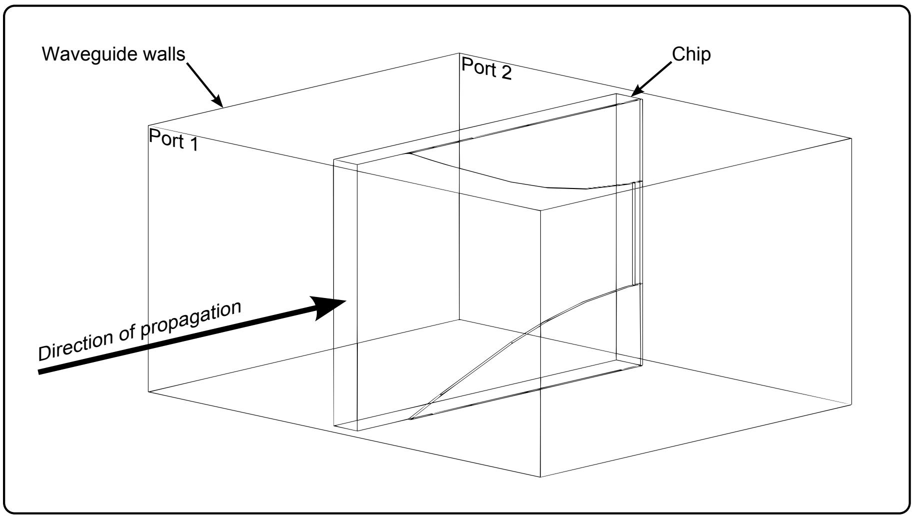

Figure 4.2: Diagram of the simulations setup. The front and rear faces of the waveguide section are the simulated ports.

response. Using this optimum offset of 180μm, a series of simulations using resistances over the range 150–500Ω in 50Ω steps were conducted. The loss factor for each was compared and showed that a resistance of 300Ω gave a slightly improved average loss and again a smoother response.

4.2.1 Modified Antenna Simulations

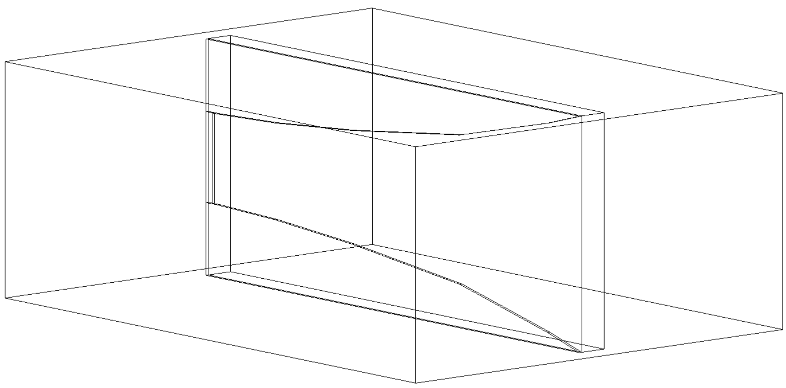

Figure 4.3: Diagram showing simulation geometry of the modified Fin-cat chip with extended antenna fins.

In order to determine how sensitive the performance of the chip is to a change in fin design, four modified antennas were tried in the simulation. The four designs of antenna are shown in figures 4.3, 4.4, 4.5 and 4.6. The

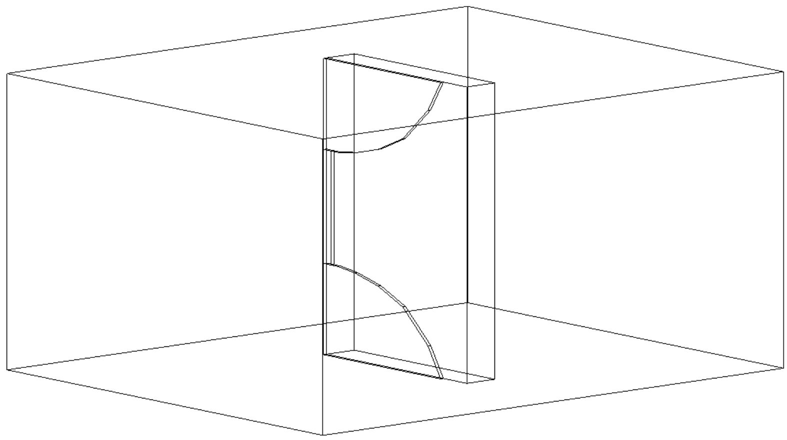

Figure 4.4: Diagram showing simulation geometry of the modified Fin-cat chip with reduced antenna fins.

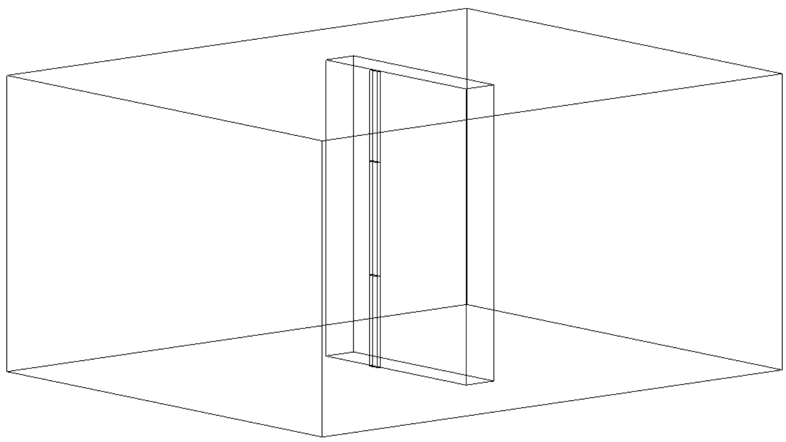

Figure 4.5: Diagram showing simulation geometry of the modified Fin-cat chip with vertical strips instead of fins.

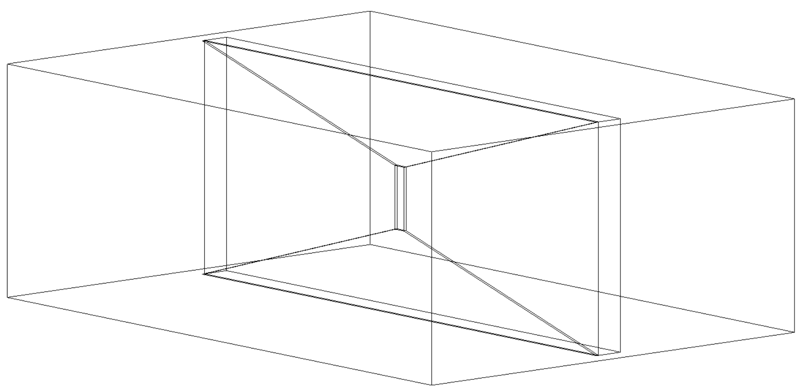

Figure 4.6: Diagram showing simulation geometry of the modified Fin-cat chip with symmetrically tapered antenna fins.

results from simulations of these alternative designs are presented in the results section.

4.3 The Simulators

In order to determine the most appropriate software for the simulation of the sensor four packages were trailed; these were Agilents EMDS 2006, COMSOL Multiphysics 3.2a, CST Studio 2009 and SEMCAD X light. The following sections provide an assessment of each package.

4.3.1 Agilent's EMDS 2006

The interface of EMDS was extremely basic with no real modelling environment. Instead, geometric shapes were entered using coordinates, which had to be determined by the user in order to correctly place shapes relative to each other. Manipulating entered models was an involved process that required entering translational matrices. This lack of usability meant that only simple models could be entered as it also lacked the ability to import geometries from third party software. Once a model had been entered, it was able to optimise the mesh and solve relatively quickly. The postprocessor, used to visualise results, was again quite basic but provided useful graphing options such as smith-charts and animated 3D slice plots. The complexity of the model required to simulate the power sensor meant that this package was unsuitable.

4.3.2 COMSOL Multiphysics 3.2a

COMSOL has a larger scope than the other packages; it provides plug-in solvers to compute thermodynamic, magnetic, acoustics and other physical phenomena. It had a similar method of entering model data as EMDS, coordinate based, but gave the option of importing CAD data from external applications. As a result, modelling was done using SolidWorks and imported into COMSOL for simulation. COMSOL is a multiplatform application running in Java, which as a result means that it tends to run out of memory prematurely in Microsoft Windows. This constrained the available memory to less than a third of what was physically available, resulting in reduced model complexity. The solver was slow and lacked a good mesh optimiser, resulting in inefficient models and therefore taking longer than necessary to solve. COMSOL tends to give meaningless error messages whenever something goes wrong causing massive delays in error correction.

4.3.3 CST Studio 2009

CST Studio was by far the best of the four. The modelling interface was good, allowing models to be entered directly using the program as well as by importing CAD data. The package had a selection of solvers available, each streamlined to provide different sets of results quickly. It also provided excellent mesh element optimisation, further decreasing its solution time. Combining adaptive mesh optimisation with the fast S-parameter solver meant that models that took hours to solve in COMSOL could be done in as little as six minutes producing similar results. Plotting and data export was good, offering everything COMSOL and EMDS did but with a better interface. CST could also plot while solving, meaning any obvious mistakes could be picked up early. Unfortunately, a license for this package was very expensive and the opportunity to gain one as part of my University Research Grant was missed.

4.3.4 SEMCAD X light

SEMCAD seems quite powerful offering a lot of control over sensors and ports but no relevant tutorials meant that there was no way of telling if these were correctly configured. Being a light edition, models were limited to one million voxels (volumetric pixels, or cubes) which meant that the simulated model was quite coarse. Limited documentation, peculiar layout and lack of useable results meant this software was not well suited for this problem.

Chapter 5

Model

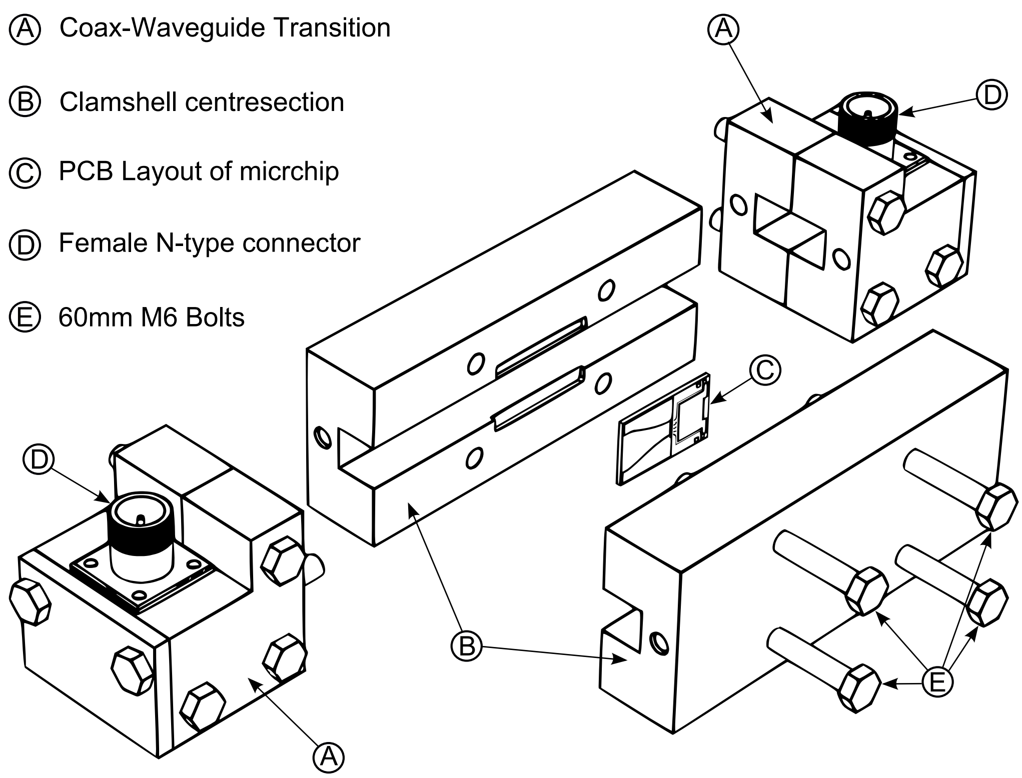

Figure 5.1: Exploded diagram of scale model built for simulation verification.

A scale model was built to verify the results of the computer simulations. Building a larger model of the chip and waveguide cavity would allow measurements to be taken at lower frequencies using equipment that was readily available.

5.1 Design

The model consists of two waveguide ports and a centre section that houses the model chip. The two ports are adapters that convert the coaxial transmission medium of the VNA to waveguide. Each of the ports and the centre section are made in halves which bolt together to form a waveguide cavity through the centre. Figure 5.1 shows the model disassembled; the groove in the centre section is used to cradle the model chip. A third centre section half was made without this groove, which will be used for calibration of the model. The model was designed using Solidworks 2008 and the cavity was etched into each of the halves using a CNC milling machine. The model is made from aluminium as it has a high electrical conductivity and is easy to work with.

The dissipating resistor for the model was done by soldering surface mount resistors between the fins of the PCB. These resistors are much thicker than the scaled thin-film resistor from the actual chip. Therefore, this will have some effect on the measured data. Surface mount resistors are essentially small ceramic bricks that have a thin layer of resistive material applied to their tops. By soldering the resistors upside down and thereby removing any offset to the path of resistance, interference is minimised.

5.1.1 Scale

The VNA is capable of making measurements between 3 kHz and 9 GHz so the scale of the model will have to be such that it will operate within this range. The thickness of the gold fins is 2μm while the thickness of copper on a standard printed circuit (PCB) board is about sixteen times thicker at 35μm. The thickness of the microchip substrate is about 100μm while again the thickness of fibreglass on a standard PCB is sixteen times thicker at 1.6mm. It was an obvious choice to make the model sixteen times larger, this would allow the chip design to be printed on a PCB and be electrically accurate. Scaling the operating frequency of the waveguide is a simple matter as it scales proportionally to the size of the cavity. The reason for this is shown in the following equation.

$$\begin{aligned} f_{c(TE_{10})} &= c\sqrt{\left(\frac{1\pi}{a}\right)^2 + \left(\frac{0\pi}{b}\right)^2} \\ &= c\sqrt{\left(\frac{\pi}{a}\right)^2} \\ &= \frac{c\pi}{a} \end{aligned} \tag{5.1}$$

This shows that the product of the TE_{10} cut-off frequency ($f_{c(TE_{10})}$) and waveguide width (a) is a constant (the speed of light times π). Therefore, if we make the scale model sixteen times larger it will operate at a sixteenth of the frequency, reducing the operational frequency range from 110–170 GHz to 6.88–10.63 GHz.

As The VNA is only able to measure up to 9 GHz, the measurements are restricted to the lower 56% of the scaled frequency band. However, the ability to make model chips simply by etching PCBs combined with an easily manufactured waveguide cavity meant that this was the most suitable choice.

5.1.2 Calibration

Because the model used waveguide, which is not the native transmission medium of the VNA, calibration was an involved process. Usually, calibration involves specifying the serial number of the calibration kit being used, which then determines the series of measurements that must be made in order to calibrate the VNA. As there was no calibration kit for the waveguide model that a custom calibration process was created. This involved defining the dimensions of the waveguide, the length of the centre section, the types of connectors. Once this was done, three types of measurements had to be specified that the VNA could use to determine the characteristics of everything between it and the waveguide ports. These three measurements were chosen as thru, line and reflect; often termed TRL. There was a problem with the definition of the line measurement that meant that data in certain areas were undeterminable. A line measurement in this case is when a section of waveguide that has a reflecting wall on one end is attached to a port. The VNA measures the length of the line by looking at the phase difference of a wave once it has been reflected back from the wall. As waves are cyclic by nature there are many possibilities as to the length of the line. To overcome this, the VNA requests that the line be a quarter wavelength long at the mid-frequency, preventing multiple length possibilities. As the centre section was over three wavelengths long at the mid-frequency there were areas in the calibration that were undeterminable. The result of this is that there are patches missing from the measured data. Had a smaller wavelength section been made, the model would have had to have been completely disassembled after calibration and reassembled with the centre sections designed to hold the chip. Doing this would drastically disturb the calibration as moving the coaxial cables has a significant effect on the measurements. However, missing segments of data in the measurements are preferable to a disturbed calibration.

5.2 Measure

Figure 5.2 shows the model with half of the centre section removed, exposing the inner waveguide cavity. To the left of the model are the two remaining halves, one to hold the model chip and one for calibration. Clamps were used to hold the model steady in order to prevent unnecessary cable movement while the centre section was disassembled.

Figure 5.2 shows the model connected to the VNA. It is being reassembled in order to take measurements.

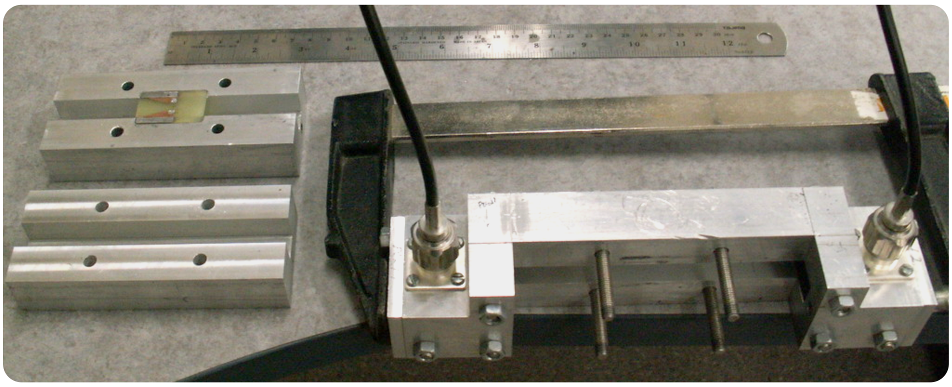

Figure 5.2: Photo of the disassembled scale model showing the waveguide cavities and PCB chip.

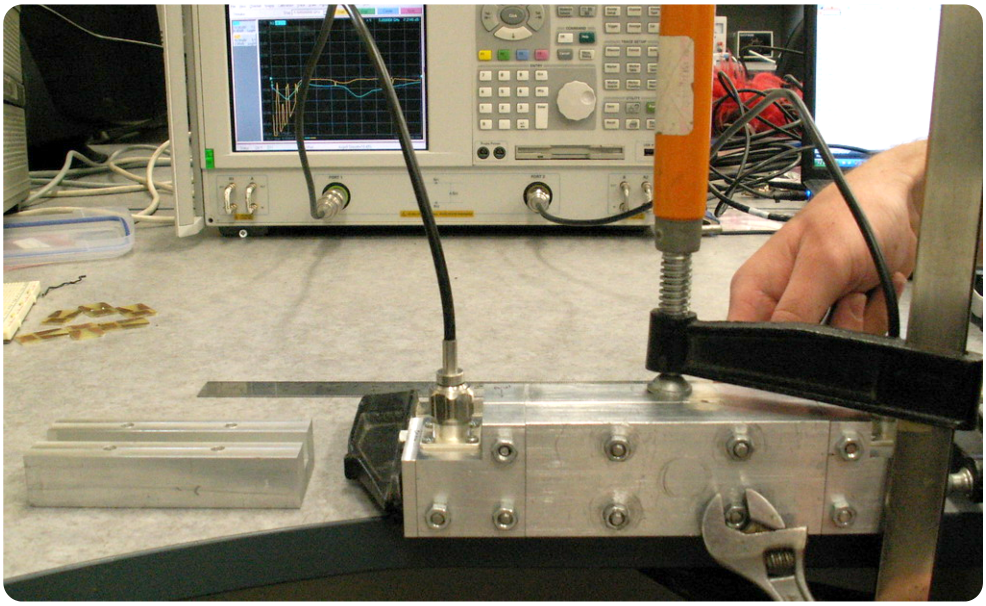

Figure 5.3: Photo of the scale model attached to VNA.

Chapter 6

Results

The results are presented in the following order: Firstly, data from the computer simulations and measurements were compared. Confidence in the simulation data depends on the agreement of these outcomes. Secondly, the results of the optimisation of the chip position within the waveguide are shown. This was based on a suggestion proposed by Adam K. Jastrzebski [11]. Thirdly, the results of the optimisation of the thin film resistance are presented. The aim of which was to further increase the match between the chip and waveguide section. Finally, simulations of alternative fin geometries are considered. These were trialled to determine whether the shape of the fins on the Fin-cat chip could be improved.

6.1 Model verification

Only the fins, resistor and substrate are present in the simulations and model, as these are the critical components for power absorption. Measurements were conducted using 124Ω, 260Ω and 480Ω resistances. An additional model measurement was conducted with no resistance in order to determine the loss attributed to the finite conductivities of the fins. Bold vertical lines on the following graphics indicate the operational frequency boundaries for WR-6 waveguide, 110 GHz and 170 GHz.

It is clear from the results that the 260Ω resistor produces the best match of

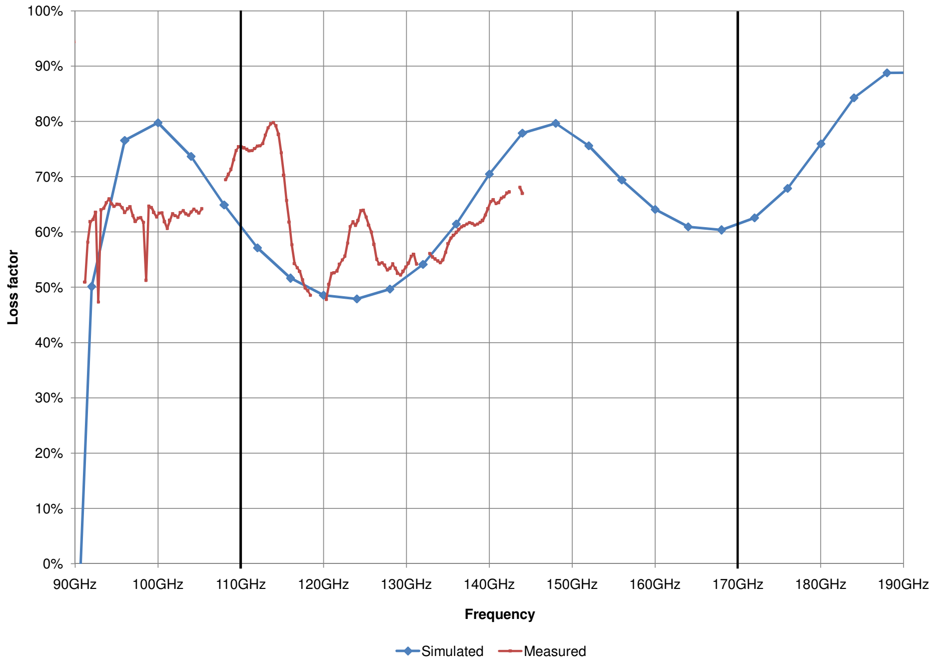

Figure 6.1: Loss factor vs. frequency comparison between measured and simulated data using a 124Ω resistor.

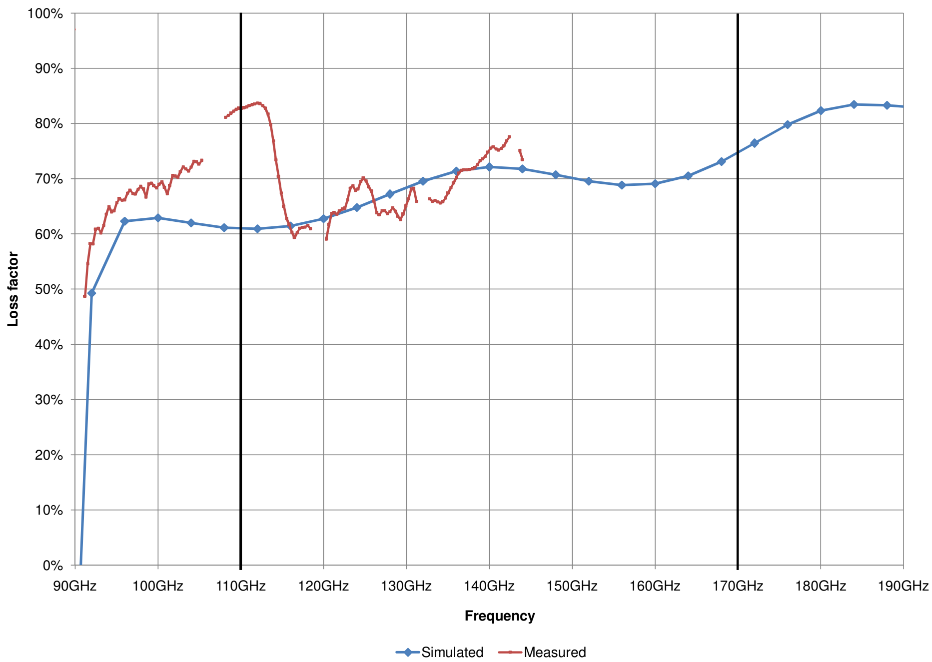

Figure 6.2: Loss factor vs. frequency comparison between measured and simulated data using a 260Ω resistor.

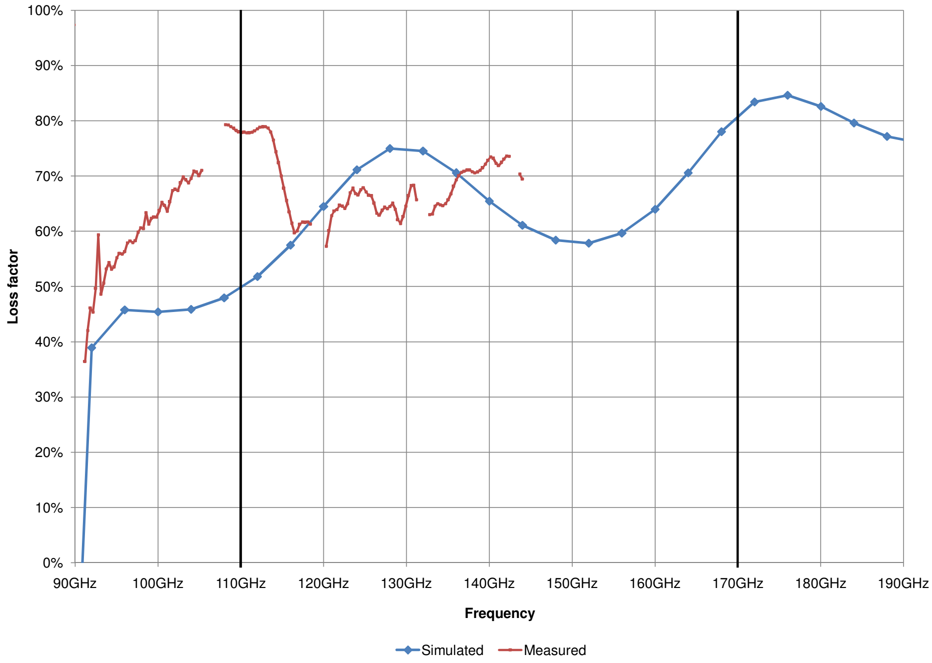

Figure 6.3: Loss factor vs. frequency comparison between measured and simulated data using a 480Ω resistor.

the three. This is evident from the smoother data produced by the simulations in figure 6.2 when compared to that in figures 6.1 and 6.3. This reduction in peaks correlates well with the measured data, which is also at its lowest in figure 6.2.

6.2 Chip offset optimisation

Offsetting the chip inside the waveguide has a large effect on the match, which can be seen in figure 6.4. As the fins are moved from the centre to 180μm of offset, there is a general improvement in both frequency response and average loss. The simulations predict that 180μm is the optimal offset result. Any further offsetting of the chip causes a decline in match and therefore reduced performance. These simulations were conducted with a thin-film resistance of 480Ω. Figure 6.5 shows the top three offsets, intended to give a clearer picture of the optimum point.

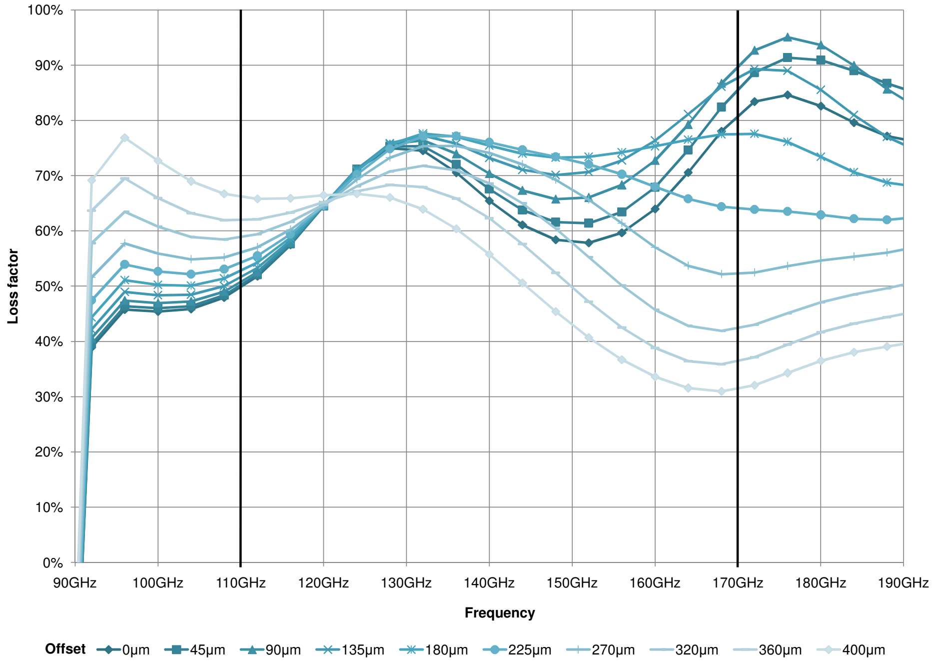

Figure 6.4: Loss factor vs. frequency across a range of chip offsets (Calculated with a 480Ω resistor).

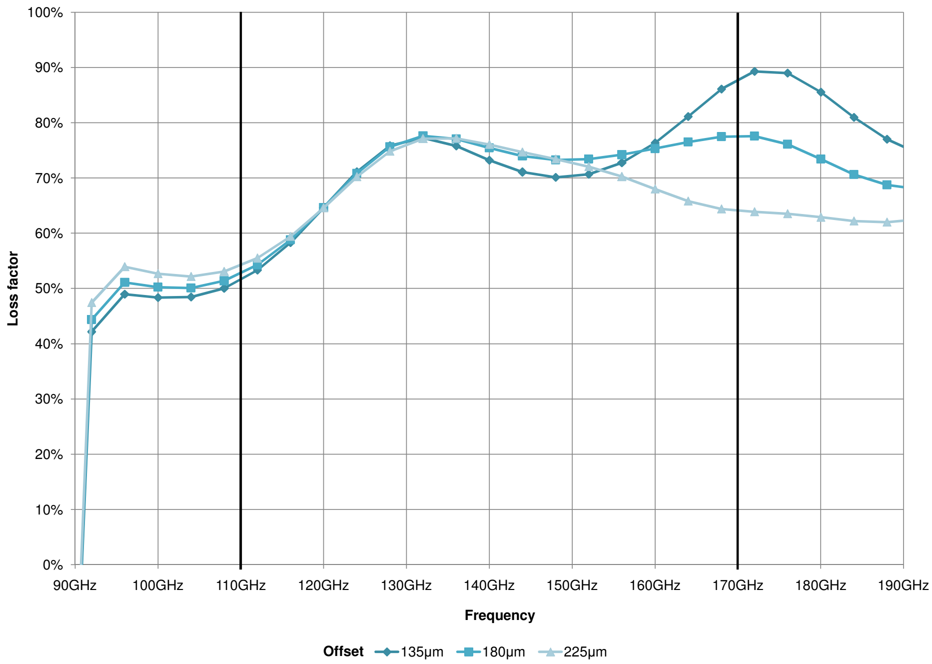

Figure 6.5: Loss factor vs. frequency for the top three offsets (Calculated with a 480Ω resistor).

6.3 Resistance value optimisation

Changing the value of the resistance, once the optimum offset (180μm) had been found, had a slightly positive effect on loss. Figure 6.6 shows the loss factor as a function of frequency using nine different resistance values. The top three of these results are shown in figure 6.7. These results predict that a resistance of approximately 300Ω is ideal.

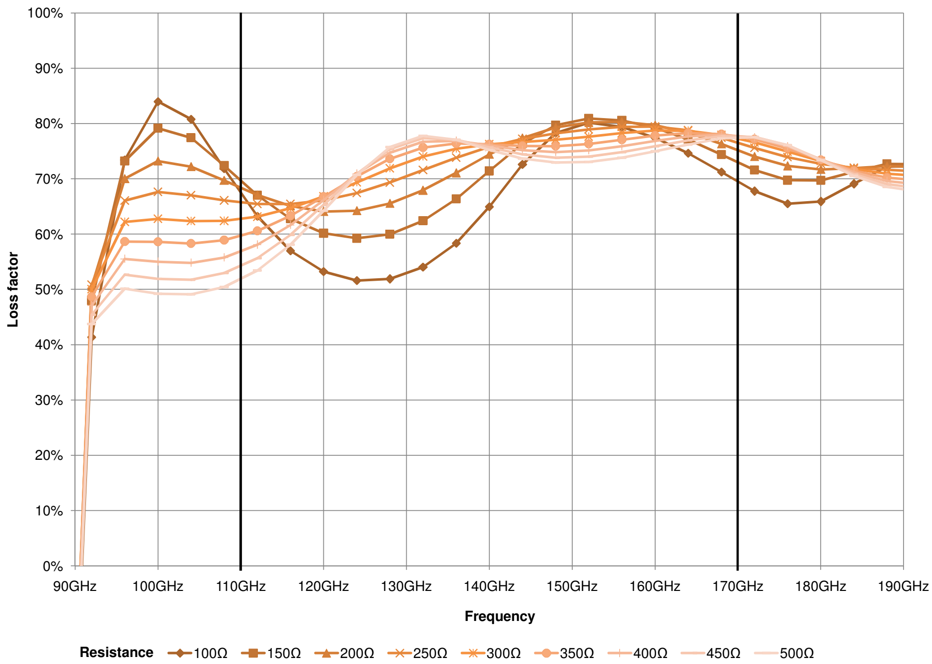

Figure 6.6: Loss factor vs. frequency across a range of resistance values (Calculated at a 180μm chip offset).

6.4 Optimisation Results

Figure 6.8 presents the overall results of optimisation predicted using the simulation software. The chip samples have resistances of 200Ω and it was initially thought they should be placed so their fins were centred in the cavity. However, by increasing the resistance to 300Ω and moving the chip 180μm to the left, performance is increased and a smoother response is attained.

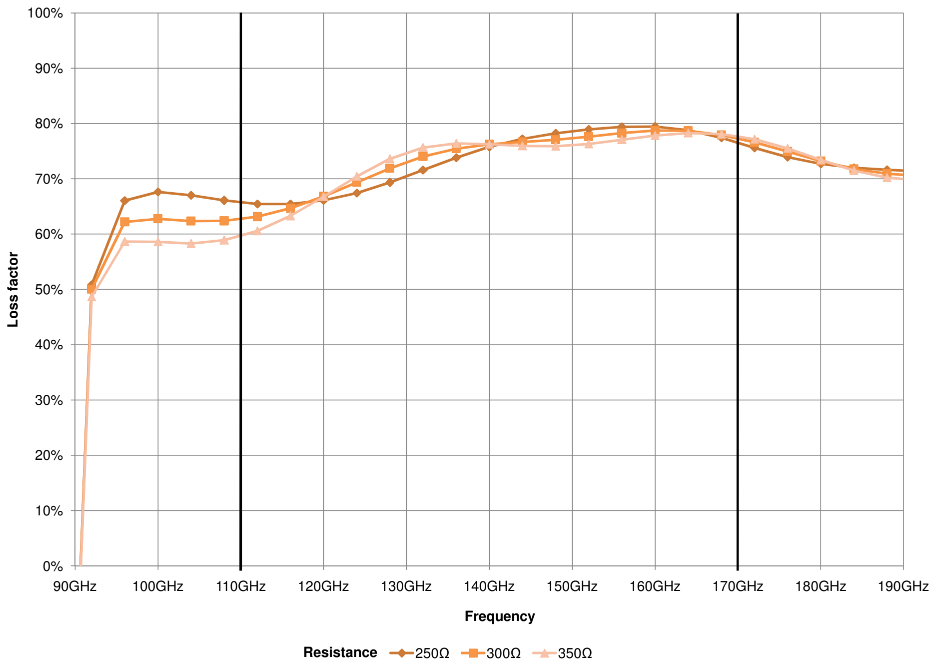

Figure 6.7: Loss factor vs. frequency for the top three resistance values (Calculated at a 180μm chip off-set).

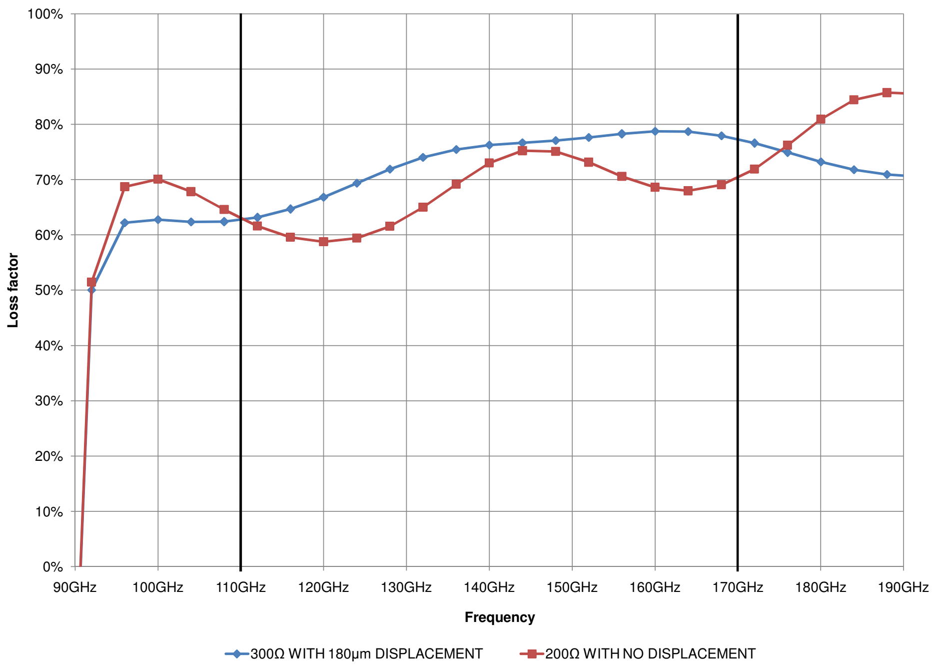

Figure 6.8: A loss factor vs. frequency comparison between an optimised sensor configuration and the original 200Ω chip positioned with the fins centred in the waveguide.

6.5 Alternate Antenna Geometries

Several alternative designs of antenna were trialled once initial simulations of the chip had been completed. These were done to see what effect the shape of the fins had on match, and consequently, on loss. The fins are all completely lossless since the simulator treats them as perfectly conductive. Therefore, any loss due to their length is not evident. Standard fins refer to the original design of the Fin-cat fins. The reduced and extended fin geometries are based on the standard Fin-cat design but have been altered in length accordingly. The geometries of these simulations can be seen in section 4.2.1.

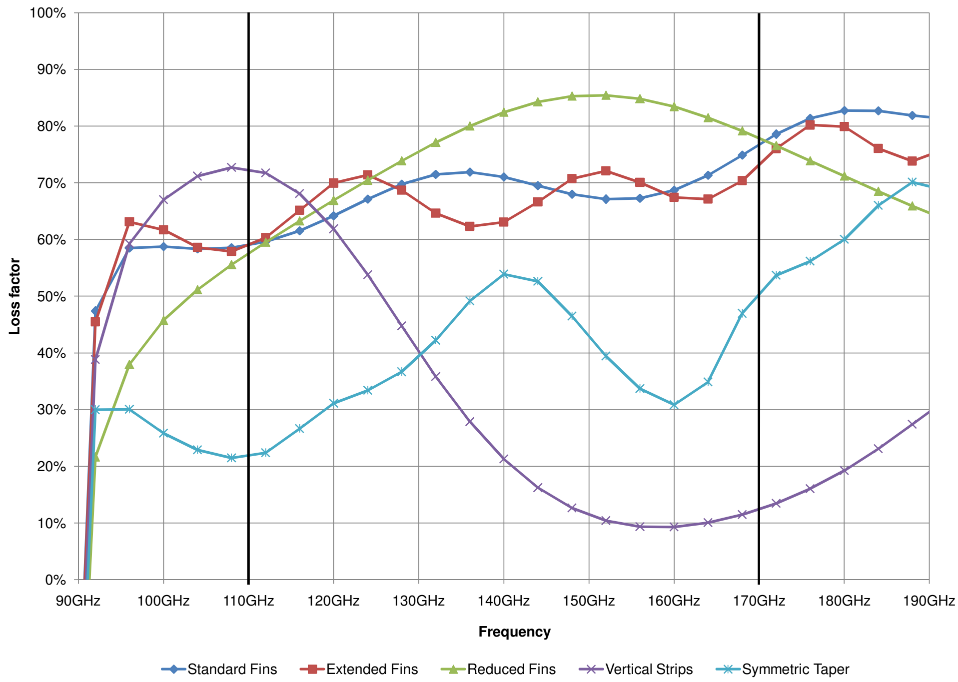

Figure 6.9: Loss factor vs. frequency comparison between optimised sensor configuration and original 200Ω centred chip.

These results suggest that the fin lengths play a small role in the overall match of the sensor.

Chapter 7

Conclusion

The goal of this investigation was to assess the concept of a uniquely designed power sensing chip placed directly in waveguide. This power sensing chip, referred to as Fin-cat, contained fin shaped antennas with which to absorb power from the waveguide.

As part of this research, I have made and measured a two-port scale model of the chip and waveguide section. I have also conducted a series of simulations of the Fin-cat chip and waveguide section. In addition to this, I have simulated a number of resistances between the fins, a range of chip offsets as well as a number of alternative fin geometries.

The designs of the chip and bulkhead are completely original. The measurements and simulations conducted over the course of this investigation have not been done before.

The results of the measurements and simulations, suggest that the concept of placing a microchip containing an antenna, resistor and thermocouples inside a waveguide in order to measure power is indeed feasible. The worst case return loss was approximately 4.3dB, equating to a loss factor of about 63%. While this return loss may not seem ideal, it is more than acceptable when operating above 110 GHz.

Importantly this study has shown that optimising the shape of the fins and the value of the resistance will not have a significant effect on the match.

This suggests that the chip substrate itself is responsible for the quality of the match.

The next step would be to build the bulkhead and test the chips. Further – more detailed – simulations would require more advanced simulation software. This could give an opportunity to further optimise the design, possibly addressing the issue of bad substrate match.

No substantial advancement in from the development of the Fin-cat chip will come with ease as this may require modification to the substrate. Hence building the sensor is the next appropriate step. Since this would be a simple matter of engineering metalwork, it should not present any significant difficulties. My investigation has shown that there are no further gains to be made without serious investment in further design work, high end simulation software, and more advanced chip fabrication technologies.

Appendix A

An alternative Concept

It was observed that the dimensions of millimetre-wave waveguide are comparable to what can be achieved in the production of the “web” patch in thermocouple-based power sensor integrated circuits, such as Jacksons. We ask the question “would it be possible to make an IC that could be mounted across the end of a section of waveguide, orthogonal to the direction of energy propagation, capturing energy using a window of resistive material?

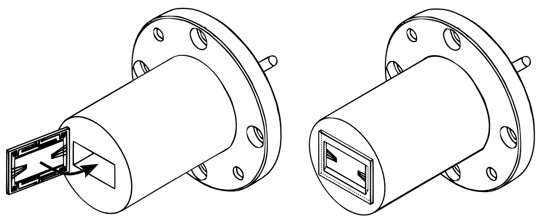

Figure A.1: Fitting the chip across the open end of a section of waveguide as an “end-cap.

Figure A.1 depicts the basic idea. An IC would be placed over the end of the guide like an oblong manhole cover, perpendicular to the incident waves. The epitaxial layers, the traditional “top” of the IC, would face outwards. The substrate would be etched away behind the energy-dissipating part of the circuit, in the method common in circuits used in coaxial systems, exposing the web to the incident waves. An obvious advantage is ease of assembly and thus manufacture, compared to the alternative of a finline approach, since the IC could be bonded in routine fashion to the rear of the bulkhead.

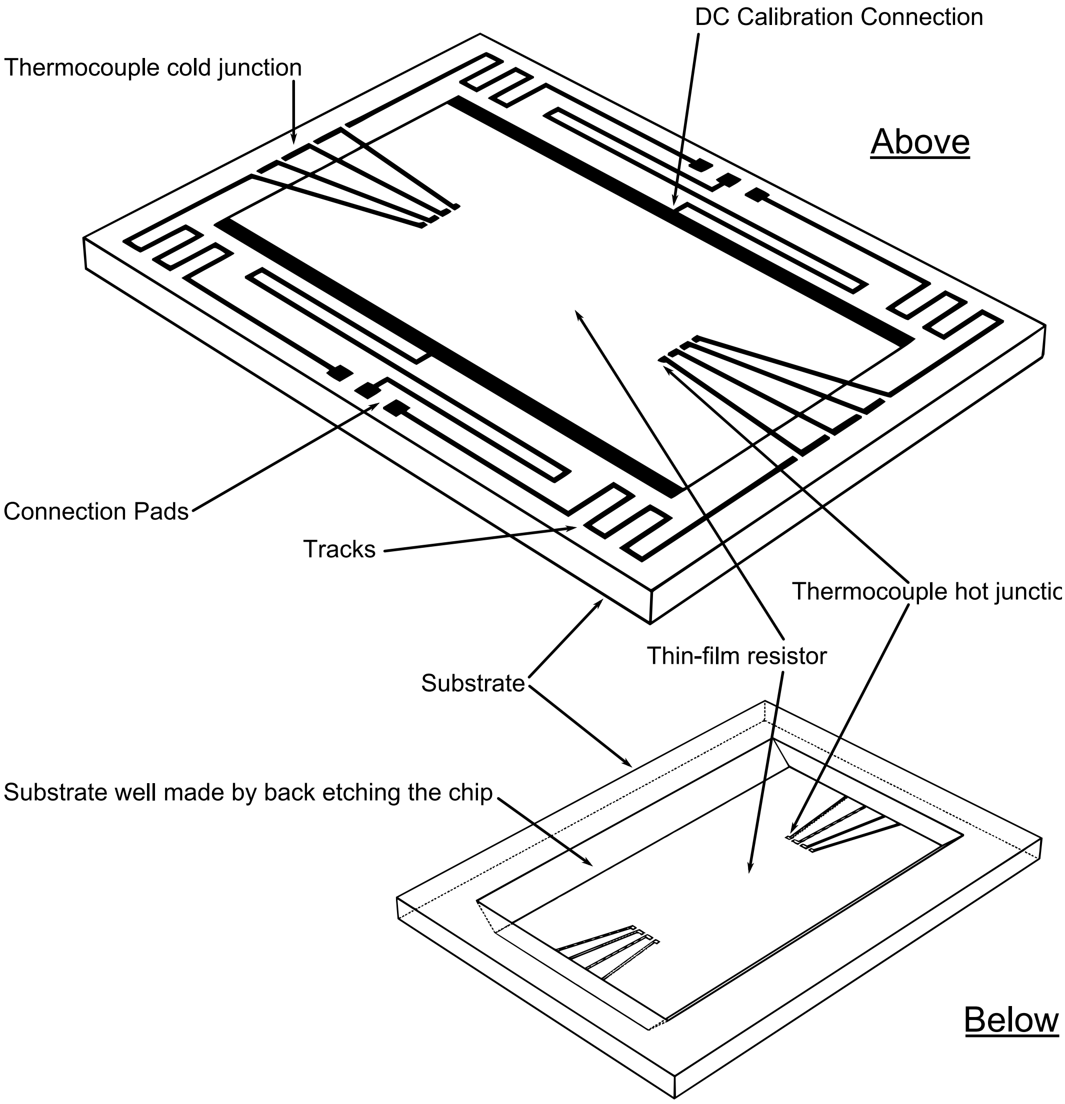

Figure A.2: Idealized diagram of the End-cap sensor IC

Figure A.2 shows the proposed design of the power sensor IC. Note that the underside of the chip has had its substrate etched away and that there is a thin film of dielectric over the 'window' that has been created. Two sets of four thermocouples reach into the centre of the film to measure the temperature rise produced by the heat dissipated in it. Note also that electrical connectivity is provided across the resistive window to allow delivery of dc (or low frequency) power to the film. This is intended as a means to permit calibration.

A.1 Mathematical Analysis

A.1.1 Reflection

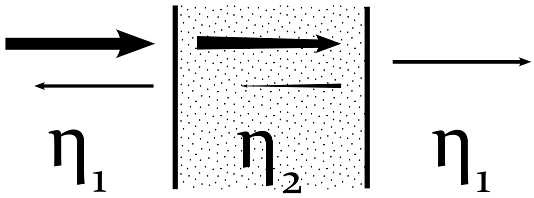

Figure A.3: Reflection and transmission at the web boundary and absorption in the web film itself.

Reflections are caused by a mismatch of impedance between transmission media. Our situation is depicted in figure A.3. In order to minimise reflection from the surface of the film, its characteristic impedance (η_2) should match that of the waveguide (η_1) as closely as possible. The fraction of energy that is reflected at a boundary is called the *reflection coefficient* (Γ), or sometimes S_{11} [16]. This presents a challenge as the characteristic impedance of the waveguide changes depending on its frequency of operation.

$$\Gamma \equiv \frac{\boldsymbol{E_r}}{\boldsymbol{E_i}} = \frac{\eta_2 - \eta_1}{\eta_2 + \eta_1} \tag{A.1}$$

Power density is proportional to the square of the electric field ($\boldsymbol{E}$) and the reflected power density (P_r) is related to the incident power density (P_i) by

$$P_r = |\Gamma|^2 P_i \tag{A.2}$$

Therefore, by conservation of energy the transmitted power is equal to

$$P_t = \left\{1 - |\Gamma|^2\right\} P_i \tag{A.3}$$

This represents the amount of power transmitted from the first medium to the second. Setting the input power (P_i) to unity and substituting equation A.1 into equation A.3 gives the fractional transmittance of power (t_{frac}) between media

$$
\begin{aligned}
t_{frac} &= \left\{1 - \left|\frac{\eta_2 - \eta_1}{\eta_2 + \eta_1}\right|^2\right\} \times 1 \\
&= \frac{1}{1} - \frac{(\eta_2 - \eta_1)^2}{(\eta_2 + \eta_1)^2} \\
&= \frac{4\eta_1\eta_2}{(\eta_2 + \eta_1)^2}
\end{aligned}
\tag{A.4}
$$

The characteristic impedance of the air-filled waveguide given by:

$$
\eta_1 = \frac{Z_0}{\sqrt{1 - \left(\frac{f_c}{f}^2\right)}} \tag{A.5}
$$

where Z_0 is the impedance of free space, f is frequency and f_c is the fundamental mode (TE_{10}) cutoff frequency given by equation 2.2.

The characteristic impedance of the dielectric medium is

$$
\eta_2 = \sqrt{\frac{j\omega\mu}{\sigma + j\omega\epsilon}} \tag{A.6}
$$

where the bulk conductivity (σ) of the available dielectric is given by

$$
\sigma = \frac{1}{R_s \cdot t} \tag{A.7}
$$

The sheet resistance (R_s) of the dielectric may have a value of $250\,\Omega/\square$ and a thickness (t) of $50nm$, giving the dielectric a bulk conductivity of $80000\,(S\,m^{-1})$. The permeability (μ) and permittivity (ϵ) are products of their relative values and free space definitions.

$$
\mu = \mu_0\mu_r \tag{A.8}
$$

$$
\epsilon = \epsilon_0\epsilon_r \tag{A.9}
$$

The magnitude of the dielectric's complex impedance used in this analysis is given by

$$
|\eta_2| = \sqrt[4]{\frac{\omega^2\mu^2}{\sigma^2 + \omega^2\epsilon^2}} \tag{A.10}
$$

A.1.2 Absorption

Dissipative attenuation due to an imperfect, nonmagnetic dielectric in waveguide is given by equation A.11.[16]

$$\alpha_d = \frac{27.3\sqrt{\epsilon_r}\tan\delta}{\lambda_0\sqrt{1-\left(\frac{f_c}{f}\right)^2}} \quad (dB/length) \tag{A.11}$$

where

$$\tan\delta = \frac{\sigma}{\omega\epsilon_r\epsilon_0} \tag{A.12}$$

The loss tangent ($\tan\delta$) quantifies the extent to which a material dissipates electromagnetic energy. By rearranging and including length (d, in our case the thin-film resistor thickness) into equation (A.11) a more standard form for dielectric dissipation results:

$$\begin{aligned}
\alpha &= \frac{27.3\sqrt{\epsilon_r}\tan\delta}{\lambda_0\sqrt{1-\left(\frac{f_c}{f}\right)^2}} && (dB/length) \\
&= d\frac{27.3\sqrt{\epsilon_r}\tan\delta}{\lambda_0\sqrt{1-\left(\frac{f_c}{f}\right)^2}} && (dB) \\
&= 10\log e^{d\frac{2\pi\sqrt{\epsilon_r}\tan\delta}{\lambda_0\sqrt{1-\left(\frac{f_c}{f}\right)^2}}} && (dB) \\
&= 10\log e^{d\frac{\omega\sqrt{\epsilon_r}\tan\delta}{c\sqrt{1-\left(\frac{f_c}{f}\right)^2}}} && (dB) \\
&= 10\log e^{d\,\beta} && (dB)
\end{aligned} \tag{A.13}$$

where

$$\beta = \frac{\omega\sqrt{\epsilon_r}\tan\delta}{c\sqrt{1-\left(\frac{f_c}{f}\right)^2}} \tag{A.14}$$

By putting the equation into this form the decibel conversion can easily be removed, leaving a ratio of incident energy to output energy of the dielectric:

$$d_{ratio} = e^{d\beta} = \left(\frac{Input_{power}}{Output_{power}}\right) \tag{A.15}$$

The reciprocal is taken and the result is the fractional amount of output power i.e. power not dissipated inside the dielectric.

$$\begin{aligned} Output_{frac} &= \frac{1}{e^{d\beta}} \\ &= e^{-d\beta} \end{aligned} \tag{A.16}$$

To find the fractional amount of power dissipated in the dielectric film, conservation of energy gives:

$$\begin{aligned} d_{frac} &= 1 - Output_{frac} \\ &= 1 - e^{-d\beta} \end{aligned} \tag{A.17}$$

A.1.3 Combining and scaling

The result of section A.1.1 is equation A.4 which calculates the fractional amount of power transmitted into the dielectric, the active part of the web of the IC. The result of section A.1.2 is equation A.17 which calculates the fraction of power dissipated by the dielectric, used to heat the temperature sensed region of the IC. Taking the product of these equations (A.4 and A.17) gives the total fractional dissipation of power (A_{frac}) by the microchip.

$$A_{frac} = t_{frac} * d_{frac} \tag{A.18}$$

To give the total dissipation value in decibels (A_{dB}) it should be of the form

$$A_{dB} = 10 * \log\left(\frac{Input_{power}}{Output_{power}}\right) \tag{A.19}$$

where $Output_{power}$ is all the power that did not get absorbed i.e. that which was reflected or passed through the film. This power is given, again by conservation of energy, by

$$\left(\frac{Input_{power}}{Output_{power}}\right) = \left(\frac{1}{1 - A_{frac}}\right) \tag{A.20}$$

The total power dissipated by the microchip (in dB) is therefore:

$$A_{dB} = 10 \log\left(\frac{1}{1 - A_{frac}}\right) \tag{A.21}$$

A.2 Results

Table A.1 compares the characteristic impedances of the two media and also shows the resulting transmission into the film. The value of η_1 is obtained from equation (A.5), and η_2 from equation (A.10). These results were calculated with a relative permittivity of unity, representing an air filled waveguide. The table indicates that only a small fraction of power will across the film interface, meaning that most of the energy is reflected back.

Table A.1: Interface transmission

Frequency (GHz)	η_1 (Ω)	η_2 (Ω)	Transmitted (%)
110	667	3.29	1.96
120	576	3.44	2.36
130	526	3.58	2.69
140	495	3.72	2.96
150	473	3.85	3.20
160	458	3.97	3.41
170	445	4.10	3.61

Table A.2 compares percentages of power transmitted into the dielectric as well as power absorbed by the dielectric. The final column combines the results, giving the total loss of power in dB. The conclusion is that the investigated materials would effectively absorb energy that enters the film, but getting it into the film in the first place presents a challenge. The match is of such poor quality that very little energy is transmitted into the film, preventing it from being dissipated.

If the relative permittivity was larger than one the situation does not improve. Figure A.4 shows the value of fractional absorption (d_{frac}) plotted against relative permittivity, note the log scale for permittivity. It is obvious that the absorption of electromagnetic energy is heavily affected by the

Table A.2: Total absorption

Frequency (GHz)	Transmitted (%)	Dissipated (%)	Absorption (dB)
110	1.96	93.1	0.080
120	2.36	90.0	0.093
130	2.69	87.8	0.104
140	2.96	86.2	0.112
150	3.20	84.9	0.120
160	3.41	84.1	0.126
170	3.61	83.2	0.132

dielectric's relative permittivity (ϵ_r). It is therefore necessary to determine the permittivity of the dielectric medium, perhaps by way of [7], in order to evaluate the electromagnetic performance of the design with certainty.

By increasing the characteristic impedance of the dielectric, a higher power transmission across the interface would result. This can be done by choosing a material with a lower bulk conductivity, or perhaps by altering the geometry of the dielectric layer itself.

Realising that a change of impedance may increase power transmission into the dielectric, the idea was investigated further. Altering the bulk conductivity of the dielectric has very little effect on the total dissipation of power as any gain made in dissipation was offset by a degradation of transmittance and vice-versa. This is shown in figure A.5. In order to increase performance, a very thick film with bulk conductivity much lower than is normally used in IC fabrication would be required.

A.3 Conclusion

A fundamental problem arises in selecting the active dielectric layer in order to obtain effective power absorption. The absorbing layer requires a few skin

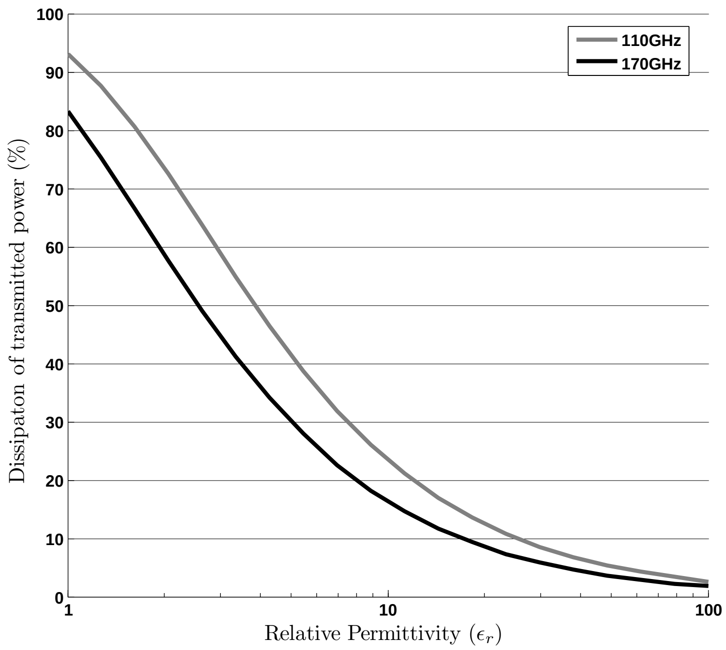

Figure A.4: Plot of the fraction of the power dissipated as a function of the relative permittivity of the dissipating medium, for the endpoints of the range of frequencies.

depths to capture energy. If the material were to be able to capture the energy in the thickness of an epitaxial layer, it would be so conductive that it would reflect most of the incident energy. In other words, we do not believe it is possible to obtain a practical material that will absorb frequencies in the 100–300 GHz range and yet be thin enough for epitaxial processing.

The bulk conductivity of a suitably absorbing layer would cause it to reflect almost all incident power back towards the source. It has been shown that altering the bulk conductivity of this layer in an attempt to reduce these reflections will not improve the overall performance of the sensor. With typical materials and thicknesses found in thermocouple-based monolithic circuits, the most optimistic solution gives a total dissipation of about 3% of the incident power. A dielectric thickness of 100μm with optimal bulk conductivity and permittivity values puts absorption at about 4.5dB. This thickness is more like that of the substrate than a deposited and photolithographically processed epitaxial layer.

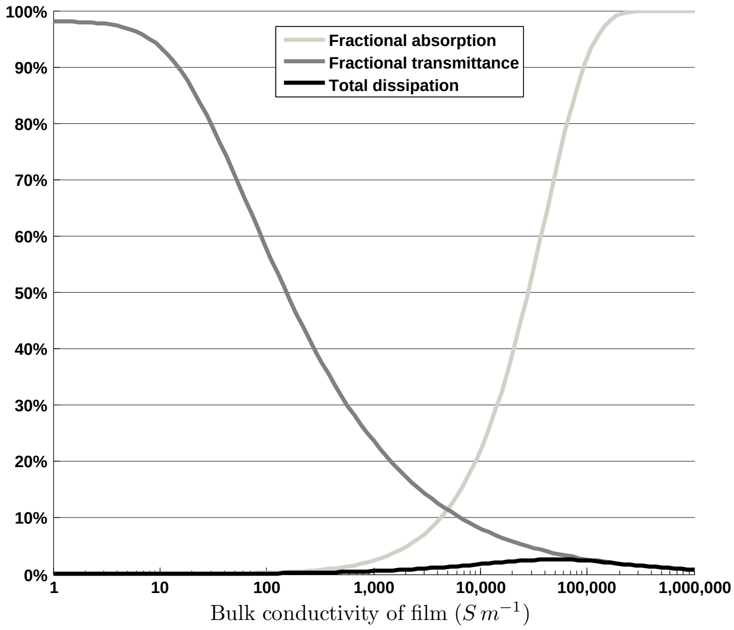

Figure A.5: Fractional absorption and transmittance vs. bulk conductivity (σ) for a relative permittivity of unity.

Appendix B

Programming the Network Vector Analyser (Agilent E8358A)

An adaptation of Prof. Scott's AgilentIO GPIB code for interfacing with the E8358A VNA. This is written in C++ and allows the VNA to be controlled from any computer on the Waikato University network.

```
#include <NEWutility.h>
#include <fstream>
#define LBUFLEN 4096

main(int argc, char* argv[])
{
//Decare variables
char busname[32];
char cmd[BUFLEN];
char cat[BUFLEN];
char fstart[10];
char fstop[10];
double freqdev;
int visanum;
int narg;
int addr;
int npts;
int xferbytes;
int i;
char flag;

//Check input paramters
if(argc < 3)
{
fprintf(stderr,"Usage: \n E8358 [GPIB Device #] [address (1-30)] [Number of points] [StartFreq] [StopFreq]");
exit(1);
}
else fprintf(stdout,"    You have entered %d argument(s)\n",argc - 1);

/***************************************** ARGUMENTS **************************************************/
narg=0; //sets narg to 0

strcpy(busname,"GPIB"); //copys the chars "GPIB" into the variable busname
visanum = atoi(argv[++narg]); //gets GPIB number from user input e.g. 13 (meaning GPIB13)
if(visanum>255 || visanum<0) err("Bad GPIB number given in VISA#");
sprintf(cmd, "%d", visanum); //puts the visa number as a decimal into cmd string
strcat(busname, cmd);
addr = atoi(argv[++narg]);
npts = atoi(argv[++narg]);

strncpy(fstart,argv[++narg],10);
strncpy(fstop,argv[++narg],10);

//fstart = argv[++narg];
//fstop = argv[++narg];

fprintf(stdout,"    Program will connect to: GPIB%d\n",visanum);
fprintf(stdout,"    Program will use address: %i\n\n",addr);

/************************************ CONNECTS TO THE MACHINE ******************************************/

// open the interface
msg("Opening the interface... ");
OpenVISA(&defaultRM);
// open session to device
sprintf(cmd, "%s::%d::INSTR", busname, addr);
nwa = OpenDevice(defaultRM, cmd); //Assign "nwa" to be the VNA.

/******************************** DEVICE OPENED AND READY TO USE **************************************/

setTMO(nwa,10000); //Set timeout to 10s
bclear(nwa);
```

```
// check instrument
msg("Talking to the NWA... \n");

fprintf(stdout," Buffer length is: %d\n",BUFLEN);

systerr(nwa);

wbstr(nwa,"*IDN?\n");

rbstr(nwa, cmd, BUFLEN);
fprintf(stdout,"    You have connected to: %s\n",cmd);


//Reset the current configuration
//wbstr(nwa,"SYSTem:FPRESET\n");


//Swap out CST file.
fprintf(stdout,"Dumping instrument CST file to 'C:\\Program Files\\Agilent\\Network Analyzer\\Documents\\cstemp.cst'\n");

//Check if temp file already exists
fprintf(stdout,"Checking for old temp file...\n");

wbstr(nwa,"mmemory:catalog?");
flag = 0;
for(i=0; i<1; i++)
{
rbstr(nwa,cmd,BUFLEN);
if(NULL != strstr(cmd,"cstemp.cst"))
{
flag = 1; //Delete old file.
fprintf(stdout"Found old cstemp.cst file. Will delete.");
}
}
if(flag)
{
fprintf(stdout,"Deleting old CST temp file");
wbstr(nwa,"mmemory:delete 'c:\\Program Files\\Agilent\\Network Analyzer\\Documents\\cstemp.cst'\n");
}
msg("Saving current CST file");
wbstr(nwa,"mmemory:store:cstate 'c:\\Program Files\\Agilent\\Network Analyzer\\Documents\\cstemp.cst'\n");

wbstr(nwa,"mmemory:load:cstate 'C:\\Program Files\\Agilent\\Network Analyzer\\Documents\\mj22.cst'\n");

fprintf(stdout,"got here3\n");

systerr(nwa);

/*
if(systerr(nwa))
{
fprintf(stderr,"Catalog of files found:\n");
wbstr(nwa,"mmemory:catalog?\n"); rbstr(nwa,cmd,LBUFLEN);
fprintf(stderr,"%s\n",cmd); //??
err("Could not load .cst file");
}
else
{
msg("Sucessfully loaded 'C:\\Program Files\\Agilent\\Network Analyzer\\Documents\\mj22.cst'\n");
}
*/
```

```
fprintf(stdout,"got here2\n");

//Create S21 Measurment
//wbstr(nwa,"CALCulate1:PARameter:DEFine \"mj22_S21\",S21\n");
//fprintf(stdout,"    Created S21 Measurment\n");

wbstr(nwa,"calculate1:parameter:catalog? \n");
rbstr(nwa,cat,BUFLEN);


if(NULL==strstr(cat,"mj22_S11"))
{ // Create the S11 measurement
sprintf(cmd,"calculate1:parameter:define \"mj22_S11\",S11 \n");
wbstr(nwa,cmd);
fprintf(stdout,"Created S11 Measurment, mj22_S11\n");
}
if(NULL==strstr(cat,"mj22_S22"))
{ // Create the s22 measurement
sprintf(cmd,"calculate1:parameter:define \"mj22_S22\",S22 \n");
wbstr(nwa,cmd);
fprintf(stdout,"Created S11 Measurment, mj22_S22\n");
}
if(NULL==strstr(cat,"mj22_S12"))
{ // Create the S12 measurement
sprintf(cmd,"calculate1:parameter:define \"mj22_S12\",S12 \n");
wbstr(nwa,cmd);
fprintf(stdout,"Created S11 Measurment, mj22_S12\n");
}
if(NULL==strstr(cat,"mj22_S21"))
{ // Create the s21 measurement
sprintf(cmd,"calculate1:parameter:define \"mj22_S21\",S21 \n");
wbstr(nwa,cmd);
fprintf(stdout,"Created S11 Measurment, mj22_S21\n");
}

fprintf(stdout,"got here");

//Turn on window 1
//wbstr(nwa,"DISPlay:WINDow1:STATe ON\n");
//fprintf(stdout,"    Turned window on ");

//Put trace into window1 and feed it from the measurment
wbstr(nwa,"DISPlay:WINdow1:TRACe1:FEED 'mj22_S11'\n");

//Setup channel for single sweep trigger
wbstr(nwa,"INITiate:CONTinuous OFF;*OPC?\n");
rbstr(nwa,cmd,BUFLEN);

wbstr(nwa,"SENSe1:SWEep:TRIGger:POINt OFF\n");

//Set channel parameters
sprintf(cmd,"SENSE1:SWEEP:POINTS %i\n",npts);
wbstr(nwa,cmd);
sprintf(cmd,"SENSE1:FREQUENCY:STOP %s\n",fstop);
wbstr(nwa,cmd);
sprintf(cmd,"SENSE1:FREQUENCY:START %s\n",fstart);\
wbstr(nwa,cmd);
sprintf(cmd,"CALCULATE1:FORMAT MLOG\n");
wbstr(nwa,cmd);
```

```
//Trigger channel
wbstr(nwa,"INIT;*OPC?\n");
rbstr(nwa,cmd,BUFLEN);

fprintf(stdout,cmd);
fprintf(stdout,"\n    RESULTS:\n");

//Select measurment to read data from
wbstr(nwa,"CALCULATE1:PARAMETER:SELECT 'mj22_S21'\n");

wbstr(nwa,"FORMAT ASCII\n");
wbstr(nwa,"CALCULATE1:DATA? FDATA\n");

ofstream file("Output.txt");



for(int i=0; i<npts; i++)
{
rbstr(nwa,cmd,20);
fprintf(stdout,"%s\n",cmd);
cmd[19] = '\n';
file << cmd;
}

//Return device to continuious sweep mode.
wbstr(nwa,"INITiate:CONTinuous ON;*OPC?\n");
rbstr(nwa,cmd,BUFLEN);



viClose(nwa);
viClose(defaultRM);
msg("\r\n    Done.");
     return(0);

}
```

Appendix C

Newspaper article

NEWS

MAKING WAVES: Waikato University electronics professor Jonathan Scott with masters student Mark Jones who is working on an accurate way of measuring terahertz.
Photo: SHANE MORTON

Riding the wave

By GEOFF LEWIS

WAVES are funny things, there are waves on the shore, waves in hair and even the Mexican wave.

But out there in the environment there are lots of waves and humans are naturally equipped to apprehend only a limited section of them – visible light, sound waves within the range of human hearing and sunburn. Outside that there is a whole zoo of waves and people go about their daily lives blissfully unaware of their existence.

In the past century or so, with the advances in science and technology, a far greater part of what is called the electromagnetic spectrum is now understood.

Waves in the spectrum are described by their frequency and range from waves of thousands of kilometres, or extremely low frequency – the African elephants of the electromagnetic spectrum – through to the ants and micro-organisms in the form of ultraviolet, x-rays and gamma rays with wave-lengths smaller than atoms. Not far down the list of the smaller waves can be found the as-yet not fully used kingdom of terahertz, which fit between the zones of microwaves and infrared radiation.

They have great potential in analysis of materials and imaging and have become increasingly the focus of interest since the 9/11 terrorist attacks in their application in airport security devices able to detect concealed weapons. That's where Waikato University science masters student Mark Jones and his supervisor electronics Professor Jonathan Scott come into it.

Mark, 24, is building an accurate measurement device for terahertz waves. In this he is funded by a $43,000 grant from the California-based Agilent Foundation.

The grant is a portion of $US1.7 million given internationally by the Hewlett-Packard spin-off to work on ways of accurately measuring terahertz.

As Professor Scott points out, devices using terahertz have significant potential in analysing substances. Existing instruments capable of measuring terahertz energy are uniformly expensive and of dubious accuracy.

He draws the analogy of the tricorder – the fantastic instrument used as a sensing device by landing parties on alien worlds in the sci-fi series Star Trek, as an example of what a terahertz-measuring instrument could do.

"It's prime application would be in the analysis of chemicals using molecular resonance.

"The reason people can see rust, for instance, is because it resonates at a wave length we can see as visible light."

Professor Scott said a terahertz-measuring device could be used for things like detecting chemicals and biological material in samples of water, through to cancers.

Figure C.1: A cutout from the local newspaper.

References

[1] GUNTHER BEGEMANN. An x-band balanced fin-line mixer. *IEEE TRANSACTIONS ON MICROWAVE THEORY AND TECHNIQUES*, MTT-26(12), December 1978.

[2] ADALBERT BEYER. Analysis of the characteristics of an earthed fin line. *IEEE TRANSACTIONS ON MICROWAVE THEORY AND TECHNIQUES*, MTT-29(7), July 1981.

[3] J. Capwell, T. Weller, D. Markell, and L. Dunleavy. Automation and real-time verification of passive component s-parameter measurements using loss factor calculations. *Microwave Journal*, 47(3), March 2004.

[4] J. de Mingo, A. Moliner, and A. Comerbn. Waveguide-to-coupled fin-line transition in ka band. *IEEE MICROWAVE AND GUIDED WAVE LETTERS*, 6(10), October 1996.

[5] Hans Delfs and Tilman Betz. Power measuring sensor for measuring high-frequency power. Other, 06 1988. EP 0223163/B1.

[6] Kenneth R. Demarest. *Engineering Electromagnetics*. Prentice Hall, 1998.

[7] Mukesh C. Dimri, V. K. Tripathi, Subhash C. Kashyap, Y. H. Jeong, and Dinesh C. Dube. Theoretical modeling and experimental verification of the permeability measurements of thick films at microwave frequencies. *IEEE Transactions on Instrumentation and Measurement*, 58(9), September 2009.

[8] Akihiko Hirata, Toshihiko Kosugi, Hiroyuki Takahashi, Ryouichi Yamaguchi, Fumito Nakajima, Tomofumi Furuta, Hiroshi Ito, Hirohiko Sugahara, Yasuhiro Sato, and Tadao Nagatsuma. 120-ghz-band millimeter-wave photonic wireless link for 10-gb/s data transmission. *IEEE TRANSACTIONS ON MICROWAVE THEORY AND TECHNIQUES*, 54(5), May 2006.

[9] Shinichi Honma and Naohisa Uehara. Millimeter-wave radar technology for automotive application. Technical Report, June 2001.

[10] Weldon H. Jackson. A thin-film semiconductor therocouple for microwave power measurements. *HP Journal*, 26(1), September 1974.

[11] Adam K. Jastrzebski. A simple condition for maximum bandwidth of a chip packaged in an mm-wave waveguide. In *European Microwave Conference, 2002. 32nd*, pages 1–4, Milan, Italy, October 2002.

[12] S. Kodato, T. Wakabayashi, Q. Zhuang, and S. Uchida. New structure for dc-60 ghz thermal power sensor. *IEEE MTT International Microwave Symposium Digest*, 2:781–874, June 1996. paper WE3F-16.

[13] Air Force Research Laboratory. Active denial system advanced concept technology demonstration. fact sheet, 2006.

[14] Pual J. Meier. Integrated fin-line millimeter components. *IEEE TRANSACTIONS ON MICROWAVE THEORY AND TECHNIQUES*, MTT-22(12), December 1974.

[15] NEETS. Naval electrical engineering training series: Module 11 - microwave principals. World Wide Web electronic publication, 1998.

[16] Peter A. Rizzi. *Microwave Engineering: Passive Circuits*. Prentice Hall, 1988.

[17] Sloan D. Robertson. Recent advances in finline circuits. *IRE TRANSACTIONS ON MICROWAVE THEORY AND TECHNIQUES*, 1956.

[18] Atsugi (JP) Setsuo Kodato. Wide-band rf signal power detecting element and power detecting device using the same. Patent, 02 2003. US 6518743.

[19] David M. Sheen, Douglas L. McMakin, and Thomas E. Hall. Three-dimensional millimeter-wave imaging for concealed weapon detection. *IEEE TRANSACTIONS ON MICROWAVE THEORY AND TECHNIQUES*, 49(9), September 2001.

[20] Agilent Technologies. Fundamentals of RF and Microwave Power Measurements, 1997. Agilent Technologies Application Note 1449-2, 2003, from HP Application Note AN64-1, 1977, revised 1997.

[21] Pin J. Wang, Jong S. Kim, and Chin C. Lee. Direct silver to copper bonding process. *Journal of Electronic Packaging*, 130(4), December 2008.